Salp Swarm Optimization Algorithm based MPPT Design for PV-TEG Hybrid System under Partial Shading Conditions

Bo Yang[a], Shaocong Wu[a], Jianxiang Huang[b], Zhengxun Guo[a,*], Jiarong Wang[a], Zijian Zhang[a], Rui Xie[a], Hongchun Shu[a], Lin Jiang[c]

[a]Faculty of Electric Power Engineering, Kunming University of Science and Technology, 650500 Kunming, China;

[b]Kunming Bureau of CSG EHV Transmission Company, 650217, Kunming, China;

[c]Department of Electrical Engineering and Electronics, University of Liverpool, L69 3GJ Liverpool, UK.

[*]Corresponding author: Zhengxun Guo, e-mail: ZhengxunGuo@outlook.com

Abstract: This paper proposes an innovative strategy to integrate thermoelectric generator (TEG) and photovoltaic (PV) systems, aiming to enhance energy production efficiency by addressing the significant waste heat generated during traditional PV system operation. Additionally, photovoltaic-thermoelectric generator (PV-TEG) hybrid system encounters the dual challenge of partial shading conditions (PSC) and non-uniform temperature distribution (NTD). Thus, salp swarm optimization (SSA) is introduced to simultaneously tackle the negative impacts of PSC and NTD. In contrast to alternative meta-heuristic algorithms (MhAs) and conventional mathematical approaches, the streamlined and effective optimization mechanism inherent to SSA affords a shorter optimization time, while mitigating the risk of the PV-TEG hybrid system's optimization outcomes being confined to local maximum power points (LMPP). Furthermore, the optimization performance of SSA for PV-TEG hybrid systems is assessed via four case studies, including start-up test, stepwise variations in solar irradiation at constant temperature, stochastic change in solar irradiation, and field measured data for typical days in Hong Kong, in which simulation results show that SSA evinces unparalleled global exploration and local search capabilities, yielding heightened energy output (up to 43.75%) and effectively suppressing power fluctuations in the PV-TEG hybrid system (as evidenced by ΔV^{avg} and ΔV^{max}).

Keywords: Salp swarm optimization algorithm, PV-TEG hybrid system, maximum power point tracking, partial shading conditions, non-uniform temperature distribution

Nomenclature

Variables		$\boldsymbol{T_{av}}$	Average value of T_{hs} and T_{cs}, °C
$\boldsymbol{V_{PV}}$	PV output voltage, V	$\boldsymbol{\mu}$	Thomson coefficient, K/Pa
$\boldsymbol{I_{PV}}$	PV output current, A	$\boldsymbol{\Delta T}$	Thermal differential between the hot and cold sides, °C
$\boldsymbol{I_g}$	Cell's photocurrent, A	$\boldsymbol{T_{am}}$	Ambient temperature, °C
$\boldsymbol{I_D}$	Diode's photocurrent, A	$\boldsymbol{A_{PV}}$	The area of the PV board, m^2
$\boldsymbol{I_S}$	Cell's reverse saturation current, A	$\boldsymbol{W_s}$	Wind speed, m/s
$\boldsymbol{P_{TEG}}$	TEG system output power, W	$\boldsymbol{\alpha_0}$	Main component of Seebeck coefficient, μV/K
$\boldsymbol{V_{oc}}$	Open-circuit voltage, V	$\boldsymbol{\alpha_1}$	Rate of Seebeck coefficient variation, μV/K
$\boldsymbol{R_{TEG}}$	Internal resistance of TEG, Ω	***Abbreviations***	
$\boldsymbol{R_L}$	Resistance of load in TEG system, Ω	**AOA**	Arithmetic optimization algorithm
$\boldsymbol{V_{oci}}$	Open-circuit voltage of the *i*th TEG module, *V*	**AOS**	Atomic orbital search
$\boldsymbol{I_{RS}}$	d-q constituents of the grid current, A	**ATO**	Arithmetic trigonometric optimization algorithm
$\boldsymbol{T_{ca}}$	Cell's absolute working temperature, °C	**DA**	Dragonfly algorithm
$\boldsymbol{T_{ref}}$	Cell's reference temperature, °C	**FA**	Firefly algorithm
$\boldsymbol{S}$	Total solar irradiation, W/m^2	**GMPP**	Global maximum power points
$\boldsymbol{E_g}$	Semiconductor's bang-gap energy utilized in the cell, J	**GWO**	Grey wolf optimization algorithm
$\boldsymbol{N_p}$	Number of parallel-connected panels	**IGBT**	Insulated gate bipolar transistor
$\boldsymbol{N_s}$	Number of series-connected panels	**INC**	Incremental conductance method
$\boldsymbol{I_{sci}}$	Short-circuit current of the *i*th TEG module, A	**LMPP**	Local maximum power points
$\boldsymbol{V_{Li}}$	Voltage at the terminal of the *i*th TEG module, V	**MFO**	Moth-flame optimization algorithm
$\boldsymbol{R_{TEGi}}$	Resistance within the *i*th TEG module, Ω	**MhA**	Meta-heuristic algorithm

P_{TEGi}	Power produced by *i*th TEG, W	**MPPT**	Maximum power point tracking
$P_{TEG\Sigma}$	Overall power output produced by centralized TEG system, W	**MRA**	Mud ring algorithm
$P_{PV\text{-}TEG}$	Output power of PV-TEG hybrid system, W	**NTD**	Non-uniform temperature distribution
η_{TEG}	Thermoelectric conversion efficiency of TEG system	**PV**	Photovoltaic
$\eta_{PV\text{-}TEG}$	Production efficiency of PV-TEG hybrid system	**PV-TEG**	Photovoltaic-thermoelectric generator
PV-TEG hybrid system parameters		**P&O**	Perturb and observe algorithm
q	Electron charge, 1.60217733×10^{-19} Cb	**RSA**	Reptile search algorithm
A	p-n junction ideality factor, between 1 and 5	**SP**	Series-parallel
k	Boltzman's constant, 1.380658×10^{-23}J/K	**SSA**	Salp swarm optimization algorithm
k_i	PV cell's temp coefficient for short-circuit current, mA/°C	**TCT**	Total cross tie
R_s, R_{SH}	Resistance of PV cell in both series and shunt, Ω	**TEG**	Thermoelectric generator
α_{pn}	Seebeck coefficient disparity between two materials (P and N), μV/K	**WOA**	Whale optimization algorithm
G_T	Solar irradiance intensity, W/m^2	***SSA parameters***	
T_{hs}	Temperature on the hot side, °C	c_2, c_3	Random numbers
T_{cs}	Temperature on the cold side, °C	k_{max}	Maximum iteration number
α_0	Basic part of Seebeck coefficient, μV/K	N	Population size
α_1	Variation rate of Seebeck coefficient, μV/K	D	Dimension of optimization problems

1. Introduction

Recently, a dramatic increase of global consumption of fossil fuels, leading to a corresponding rise in waste heat emissions into the atmosphere [1]. Moreover, this indiscriminate use of fossil fuels has resulted in severe environmental pollution, prompting scientists worldwide to focus on building up renewable energy fields [2]. Inspiringly, to combat the risks of traditional fossil fuel usage, the third industrial revolution, characterized by the adoption of renewable energy, has started to take shape. A plethora of sustainable and environmentally-friendly energy sources exist, encompassing hydropower, wind power, wave energy, biomass power, solar energy, and thermoelectric power, among others [3-5]. Among them, photovoltaic (PV) power stands out as a particularly promising and efficient alternative during the transition from conventional to sustainable energy sources, due to its abundance of input energy, cleanliness, silent operation, and ease of installation [6].

Whilst PV modules can absorb the visible spectrum of solar radiation, a significant amount of excess heat generated by the infrared spectrum is lost [7], which generally damages their power generation efficiency (only from 12-18%) [8]. Fortunately, the power generation efficiency can be improved using a combination of a thermoelectric generator (TEG) and PV technology. This hybrid system, known as a photovoltaic-thermoelectric generator (PV-TEG), can harness both the light and heat generated by solar radiation to produce electricity. Its physical structure is illustrated in Fig. 1. Here, TEGs are situated beneath PV panels to absorb excess heat and cool PV modules simultaneously. Many studies report an increased efficiency of about 10% when using PV-TEG systems compared to individual PV modules [9-13].

Two primary techniques to create a PV-TEG hybrid system have been used in previous research: (1) pasting a TEG module to the bottom of the PV module [14], and calculating the temperature difference of the TEG using the heat conduction formula that has been confirmed on PV module [15]; (2) Using a spectrum separator to reflect photons that cannot be absorbed by PV system onto TEG system to generate electricity [16]. Note that this study is carried out exclusively employing the first method as its foundation, thereby demonstrating a commitment to rigor and consistency. Besides, partial shading conditions (PSC) caused by rapidly moving clouds can create issues with large PV arrays. Energy conduction in PV-TEG hybrid system means that PSC may affect not only the irradiance reception of PV modules but also the indirect heat reception of TEG modules, leading to non-uniform temperature distribution (NTD). Notably, PV arrays may exhibit multiple peaks in their power-voltage (*P-V*) curve due to PSC. Similarly, TEG arrays may have multiple local maximum power points (LMPP) due to NTD, while the global maximum power point (GMPP) is exactly one in a PV-TEG hybrid system. Hence, ingeniously using optimization methods to change their electrical operating points in real-time for maximum power point tracking (MPPT) has been the most sensible choice.

Centralized PV and TEG arrays have been chosen to study MPPT in PV-TEG hybrid systems, aiming at improving cost-effectiveness while maintaining optimum performance in recent years. In previous studies, conventional mathematical methods, such as incremental conductance method (INC) and perturbation and observation method (P&O) [17,18], have been widely used by researchers to perform MPPT of PV and TEG modules due to their advantages of high stability and simplicity. However, energy input of PV-TEG hybrid system comes from non-uniform solar radiation, which leads to more complex and obvious multiple peaks in its *P-V* curves. Therefore, MPPT of PV-TEG using mathematical methods based on derivative and step properties will easily fall into LMPP, which reduces overall production efficiency.

Moreover, topological nature of the series and parallel arrangement of PV arrays and TEG arrays enables the implementation of larger arrays, while undoubtedly increasing the optimization complexity and difficulty. Inspiringly, meta-heuristic algorithms (MhAs) have been continuously developed to solve such optimization problems [19] thanks to their strong global search ability, fast convergence speed, and low computational cost.

This work adopts a salp swarm optimization algorithm (SSA) to harvest the maximum power of PV-TEG hybrid system, which can well balance global exploration and local search. Due to both powerful and stable search mechanisms, SSA can quickly approach high-quality GMPP even with poor initial solutions.

Furthermore, the succeeding segments of this manuscript are organized in the following: Section 2 clearly describes the difficulties of combining PV system and TEG system, and provides detailed modeling for dimensional PV-TEG systems; Section 3 proposes SSA; Section 4 aims to design MPPT controllers for PV-TEG hybrid systems under PSC and NTD; Moreover, section 5 validates and analyzes the proposed models and methods under four input conditions; Finally, section 6 summarizes the full text and provides a prospect for future research in this field.

2. Mathematical modelling of PV-TEG hybrid system

Numerous hybrid strategies have been proposed to optimize utilization of both light and heat energy from solar radiation. In particular, Table 1 presents an overview of prior research on MPPT for PV-TEG hybrid systems, highlighting their distinctive connection types and methodologies.

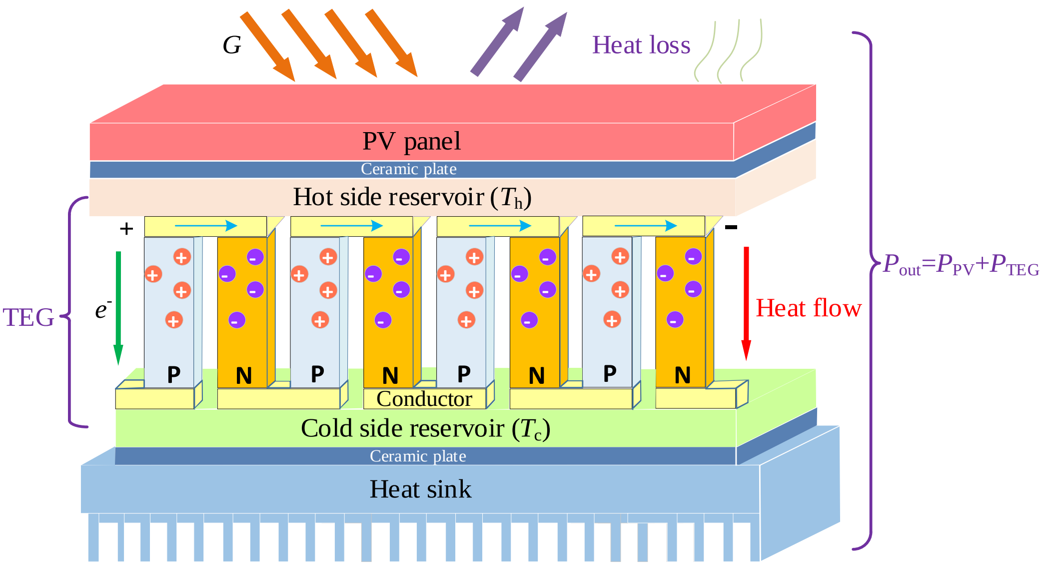

Fig. 1. Physical structure diagram of PV-TEG hybrid system.

Table 1. Chronological summaries of seven previous works related to PV-TEG hybrid system.

Literature	Year	Combination type	Combination method	Main work
Verma et al. [20]	2016	Electrical connection	PV and TEG each use an MPPT controller, while the two boost circuits are parallel	Two MPPT controllers was used to control PV module and TEG module respectively and ultimately connects the two boost circuits in parallel to collect energy.
Kwan et al. [21]	2017	Electrical connection	PV and TEG are physically connected, while a dual input boost circuit was applied.	A dual-input boost circuit was used in the MPPT design of PV-TEG.
Mirza et al. [22]	2021	Electrical connection	N.P.	Electrically connecting PV and TEG modules to achieve centralized PV-TEG hybrid system MPPT
Khan et al. [23]	2022	Electrical connection	N.P.	Electrically connecting PV and TEG modules to achieve centralized PV-TEG hybrid system MPPT
Fini et al. [24]	2022	Physical connection	PV system and TEG system are separate systems	TEG modules were glued to the bottom of PV board to absorb heat, and their annual performance was analyzed using finite element methods
Cotfas et al. [25]	2022	Electrical connection	PV-TEG hybrid module is constructed by connecting PV and TEG in series.	The electrical connection methods and MPPT methods of PV-TEG hybrid systems were systematically summarized.
Khan et al. [26]	2023	Electrical connection	PV and TEG are connected in series to build PV-TEG hybrid module, while centralized array uses one MPPT controller.	MPPT control and a data-driven fault detection algorithm are applied to enhance power generation efficiency in PV-TEG system.

*Note. N.P.: Not provided.

The primary objective of this investigation is to optimize the conversion of solar energy to electrical energy by synergistically integrating PV and TEG systems. The distinct electrical characteristics of PV and TEG systems, as current and voltage sources, respectively, are tricky obstacles in achieving MPPT. Generally, the thermal coupling of PV-TEG modules occurs through their physical connection. A comprehensive review by work [27] presented the interdependence of cell operating temperature with ambient temperature, wind speed, and irradiance, offering both implicit and explicit correlation equations. Literature [16] derived a linear correlation equation through experiments on measured data between PV module temperature, ambient temperature, and illumination. In reference [28], an effective model was proposed to estimate PV module's operating temperature relative to ambient temperature, solar irradiance intensity, and wind speed. This study conducts thermal connections between PV and TEG based on the findings of the work [27].

2.1 PV system modelling under PSC

2.1.1 Model of PV cell

Typically, an ideal PV cell consists of a photogenerated current source, parallel diodes, and series resistors, which utilize the photovoltaic effect of P-N semiconductor junctions to generate current. For specific schematic diagrams and formulas, please refer to reference [29]. Multiple PV modules are integrated with both series and parallel configurations to increase output power. The relationship between the output current and voltage of a PV array is commonly characterized as follows:

$$I_{\mathrm{PV}} = N_{\mathrm{p}} I_{\mathrm{b}} - N_{\mathrm{p}} I_{\mathrm{s}} \left(\exp\left[\frac{q}{AKT_{\mathrm{ca}}} \left(\frac{V_{\mathrm{PV}}}{N_{\mathrm{s}}} + \frac{R_{\mathrm{S}} I_{\mathrm{pv}}}{N_{\mathrm{p}}} \right) \right] - 1 \right) \tag{1}$$

where all variables mentioned above have been explained in nomenclature.

In addition, the photogenerated current I_{g} is determined by solar radiation s and T_{c}, as follows:

$$I_g = \left(I_{\mathrm{sc}} + k_i (T_{\mathrm{ca}} - T_{\mathrm{ref}}) \right) \frac{s}{1000} \tag{2}$$

where all variables mentioned above can be found in nomenclature.

Moreover, the temperature can affect the saturation current, which yields

$$I_{\mathrm{s}} = I_{\mathrm{RS}} \left[\frac{T_{\mathrm{c}}}{T_{\mathrm{ref}}} \right]^3 \exp\left[\frac{qE_{\mathrm{g}}}{Ak} \left(\frac{1}{T_{\mathrm{ref}}} - \frac{1}{T_{\mathrm{ca}}} \right) \right] \tag{3}$$

where I_{RS} and E_{g} have been explained in nomenclature.

2.1.2 PV array under partial shading conditions

PV cells are conventionally modeled as current sources in practical engineering, in which the voltage and power output are increased through series and parallel connections of PV modules, commonly referred to as total cross-tie (TCT) connections. When exposed to varying intensities of solar radiation, PV modules in a PV array exhibit different short-circuit currents. If the current generated by a particular PV module is smaller than string currents, the module undergoes voltage reversals which act as a load, absorbing the electrical energy generated by other PV modules and dissipating it as thermal energy, resulting in the hot spot effect. To mitigate this negative effect and prevent damage to the PV array, bypass diodes for each PV module are introduced, as illustrated in Fig. 2 (a). Bypass diodes will be activated to limit reverse flow of current when the PV cell receives varying irradiance. When all PV cells are under PSC, bypass diodes are turned off, as shown in Fig. 2 (b). In general, a PV array may exhibit multiple LMPPs on its *P-V* characteristic curve due to the shunting of bypass diodes to a single PV cell, and the number of LMPPs is directly proportional to the number of partially shielded individuals, as depicted in Figs. 2 (c) and (d). Notably, the voltage generated by a shielded PV cell is subject to certain limitations, as follows

$$V_{\mathrm{reverse}} = nV_{\mathrm{oc}} + V_{\mathrm{Bdiode}} \tag{4}$$

where V_{oc} is the open circuit voltage; n is the number of PV cells that are not shielded; and V_{diode} is the voltage drop on the diode.

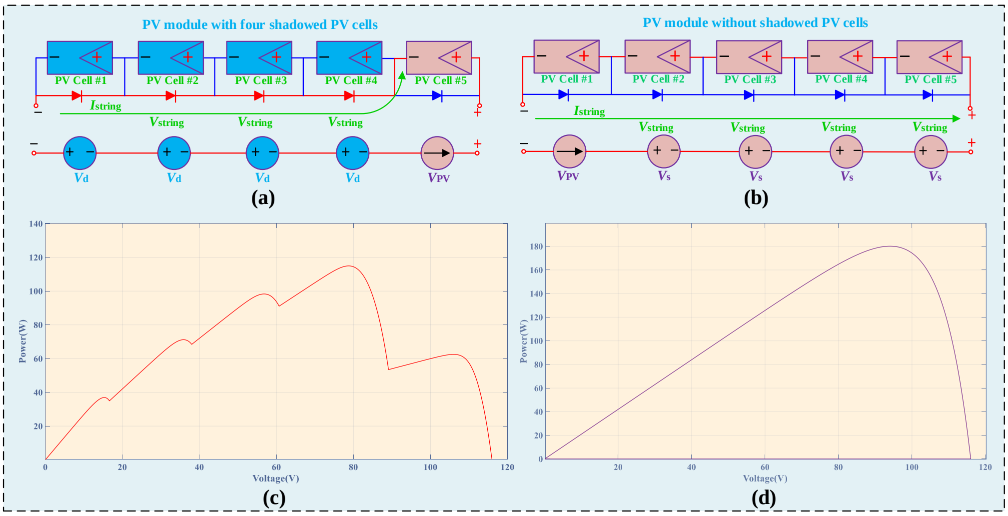

Fig. 2. Electrical characteristics of PV cell under PSC effect. (a)with shadowed PV cell; (b)without shadowed PV cell; (c)*P-V* characteristic curve of PV cell with PSC, and (d)*P-V* characteristic curve of PV cell without PSC.

2.2 Mathematical model of TEG system

2.2.1 Model of TEG individual

Figure 3 (a) illustrates the connection of multiple conductive metals in series to form a TEG module. Within this module, thermocouples composed of P-type and N-type semiconductors are positioned between hot-side and cold-side ceramic plates, generating electricity according to the Seebeck effect, as depicted in Fig. 3 (c). Besides, TEG individual can be modeled as a voltage source series resistor, shown in Fig. 3 (b). Note that the open circuit voltage V_{oc} is dependent on the temperature differential across TEG module, as expressed below

$$V_{\text{oc}} = \alpha_{\text{pn}}(T_{\text{hs}} - T_{\text{cs}}) = \alpha_{\text{pn}} \cdot \Delta T \tag{5}$$

where all explanations for mentioned parameters can be found in nomenclature.

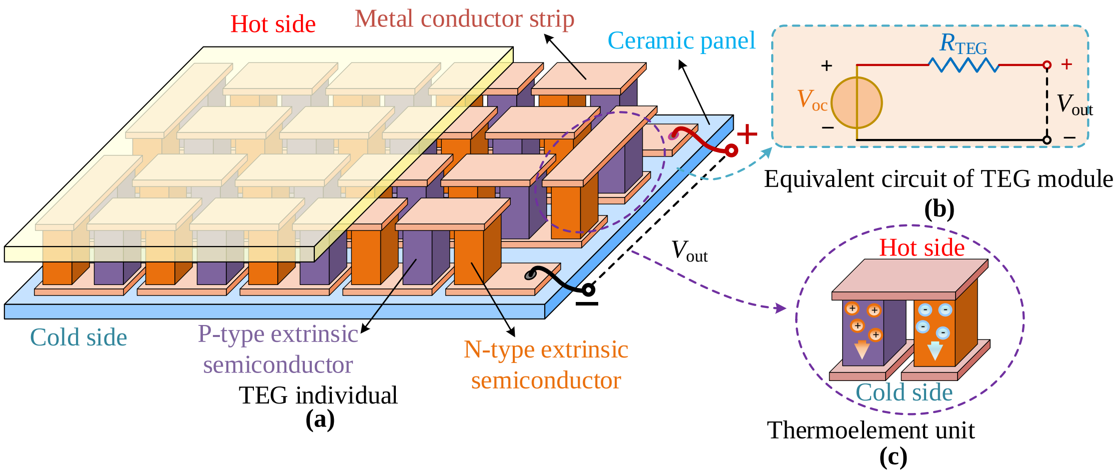

Fig. 3. Schematic of TEG module. (a)TEG internal schematic diagram; (b)Equivalent circuit of TEG module; and (c)Thermoelectric couple unit.

Here, TEG module is subject to the influence of both the Thomson coefficient and the Seebeck effect. The correlation between and the Thomson coefficient τ(v/k) can be expressed as follows

$$\tau = T_{\mathrm{av}} \frac{\mathrm{d}\alpha_{\mathrm{pn}}}{\mathrm{d}T_{\mathrm{av}}} \tag{6}$$

here, T_{av} represents the average temperature between hot and cold sides.

To enhance the precision of modeling TEG, a non-zero Thomson coefficient is utilized. As evident from Eq. (6), Seebeck coefficient is dependent on T_{av}, which can be effectively determined by

$$\alpha(T_{\mathrm{av}}) = \alpha_0 + \alpha_1 \ln\left(\frac{T_{\mathrm{av}}}{T_0}\right) \tag{7}$$

where α_0 (210μV/K) and α_1 (120μV/K) are basic part and variation rate of Seebeck coefficient, respectively.

Moreover, the output power of the TEG module can be calculated by

$$P_{\mathrm{TEG}} = \left(\alpha_{\mathrm{pn}}\Delta T\right)^2 \cdot \frac{R_{\mathrm{L}}}{(R_{\mathrm{L}}+R_{\mathrm{TEG}})^2} \tag{8}$$

where all variables mentioned above have been explained in nomenclature.

2.2.2 TEG array under NTD

Multiple TEG modules are commonly interconnected in diverse configurations to ensure adequate power output. As TEG modules are modeled as voltage sources, they increase output current and output power through parallel and series connections respectively, referred to as series-parallel (SP) topology. Similar to PV arrays, with an increase in the size of the array, each TEG module may be exposed to different temperatures. Such a mismatch may cause power losses, as illustrated in Fig. 4, in which bypass diodes are used to decrease the negative effect of a single TEG module damage while series diodes are utilized to prevent current from circulating among columns.

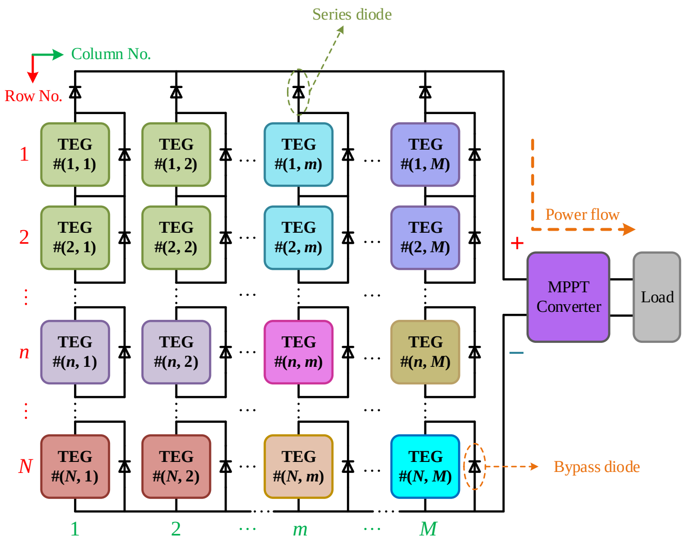

Fig. 4. TEG system structure.

By modeling a centralized array of N TEG modules in series and parallel, both efficient electricity production and refinement can be achieved, as follows:

$$I_i = \begin{cases} (V_{\mathrm{oc}i} - V_{\mathrm{L}i}) \cdot \frac{I_{\mathrm{sc}i}}{V_{\mathrm{oc}i}} = I_{\mathrm{sc}i} - \frac{V_{\mathrm{L}i}}{R_{\mathrm{TEG}i}}, \text{if } 0 \le V_{\mathrm{L}i} \le \frac{I_{\mathrm{sc}i}}{V_{\mathrm{oc}i}}, i = 1,2, \dots, N \\ 0, \text{otherwise} \end{cases} \tag{9}$$

where all variables mentioned above can be found in nomenclature.

The output power of the ith TEG module is

$$P_{\mathrm{TEG}i}=\begin{cases}V_{\mathrm{L}ii}\cdot I_i=I_{\mathrm{sc}i}V_{\mathrm{L}i}-\frac{I_{\mathrm{SC}i}}{R_{\mathrm{TEG}i}}V_{\mathrm{L}i}^2,\ \text{if } 0\le V_{\mathrm{L}i}\le\frac{I_{\mathrm{sc}i}}{V_{\mathrm{oc}i}},\ i=1,2,\ldots,N\\ 0,\ \text{otherwise}\end{cases}\tag{10}$$

where $P_{\mathrm{TEG}i}$ is the power produced by the ith TEG module.

The total output power of the TEG array equals the combined power generated by its modules, expressed by

$$P_{\mathrm{TEG}\Sigma}=\sum_{i=1}^{N}P_{\mathrm{TEG}i}\tag{11}$$

2.3 Combination of PV system and TEG system

In practical engineering, the commonly used SP connection in PV power plants is unsuitable for PSCs due to its dependence on irradiance intensity. On the other hand, TEG arrays are not affected by these conditions, making them more suitable for NTDs. Therefore, the TCT connection and SP connection are adopted to configure PV array and TEG array, respectively [30]. Furthermore, PV-TEG hybrid system is equipped with dual MPPT controllers and boost circuits to aggregate power from both arrays, as shown in Fig. 5.

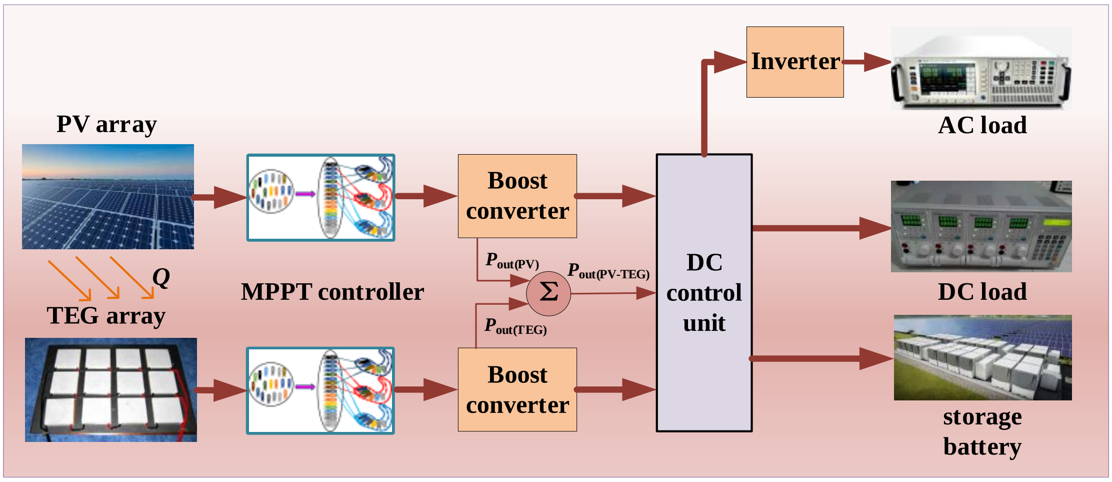

Fig. 5. Schematic illustration of MPPT for PV-TEG hybrid system.

As shown in Fig. 1, in PV-TEG hybrid system, insulating high thermal conductivity silicone resin is applied to the back plate of PV module and connected to TEG module. By installing a cooling and heat dissipation device at the cold side of TEG, the temperature of cold side can be reduced, thereby increasing the temperature difference of TEG and improving power production. Through integrated technology, the light and heat energy generated by the sun can be effectively utilized. TEG systems can not only generate electricity from the waste heat of PV systems, but also provide cooling to improve the production efficiency of photovoltaic modules. This study utilizes SSA-based MPPT technology to simultaneously achieve optimal power output for both PV and TEG subsystems, thereby improving the power generation efficiency of PV-TEG hybrid system. To achieve heat transfer between PV and TEG modules, reference [27] demonstrates that the hot side temperature in TEG is simultaneously influenced by ambient temperature T_{am}, wind speed W_{s}, and solar irradiance intensity G_{T}, which can be presented below

$$T_{\mathrm{cam}}=0.943T_{\mathrm{a}}+0.028G_{\mathrm{T}}-1.528W_{\mathrm{s}}+4.3\tag{12}$$

The total power output of the overall system is the summation of the electricity generated by both PV and TEG components, yields

$$P_{\mathrm{PV\text{-}TEG}}=P_{\mathrm{PV}}+P_{\mathrm{TEG}}\tag{13}$$

Moreover, the relationship between the power conversion efficiency of PV-TEG hybrid system and

PV system and TEG system is as follows [26]:

$$\eta_{\mathrm{PV-TEG}} = \frac{P_{\mathrm{PV}}+P_{\mathrm{TEG}}}{G_{\mathrm{T}}\times A_{\mathrm{PV}}} \tag{14}$$

where S_{PV} is PV board area.

3. Slap swarm optimization algorithm

The optimization procedure of SSA comprises of three stages: population initialization, leader position update, and follower position update [31].

(1) Population initialization

Given a search space that is a $D\times N$ Euclidean matrix $\boldsymbol{X}$ to store the positions of all salps, with D being the dimension and N being the number of populations, as follows:

$$\boldsymbol{X} = \begin{bmatrix} x_1^1 & x_2^1 & \dots & x_d^1 \\ x_1^2 & x_2^2 & \cdots & x_d^2 \\ \cdots & \cdots & \cdots & \cdots \\ x_1^n & x_2^n & \cdots & x_d^n \end{bmatrix} \tag{15}$$

Additionally, the position of each salp is determined through optimization problem's boundaries and a random number, as below

$$x_j^i = rand * \left(u_{\mathrm{b}j} - l_{\mathrm{b}j}\right) + l_{\mathrm{b}j}, i \in \{1,2,\dots,n\}, j \in \{1,2,\dots,d\} \tag{16}$$

where u_{b} and l_{b} denote the upper and lower bounds of optimization problem, and *rand* is a randomly generated number between 0 and 1.

(2) Leader location update

Upon initializing the population, the salp individuals must undergo an evaluation and ranking process based on their fitness levels. The individual exhibiting the highest fitness is appointed as the leader and assigned the top rank. Subsequently, the position update formula for the leader can be described by

$$x_j^{(1)} = \begin{cases} F_j + r_1\left(\left(u_{\mathrm{b}j} - l_{\mathrm{b}j}\right) * r_2 + l_{\mathrm{b}j}\right) & \text{if } r_3 \le 0.5 \\ F_j - r_1\left(\left(u_{\mathrm{b}j} - l_{\mathrm{b}j}\right) * r_2 + l_{\mathrm{b}j}\right) & \text{if } r_3 > 0.5 \end{cases} \tag{17}$$

$$r_1 = 2e^{-\left(\frac{4t}{T}\right)^2} \tag{18}$$

where x_j represents the jth dimension of the leader; F_j stands for the global optimal location of the jth dimension, i.e., food location; r_1 is a constant for dynamic updates; t and T denote the current and maximum iterations, respectively; r_2 and r_3 are random numbers in the range of 0-1, which control the update method of the leader.

(3) Follower location update

During the movement or hunting behavior of each salp, the followers in the population will be influenced by the front and rear individuals, thereby advancing in a chain state in sequence. The displacement process of the followers can be expressed by:

$$X = \frac{1}{2}at^2 + v_0 t \tag{19}$$

where a and v_0 represent the acceleration and initial velocity of the salp individual, respectively.

4. Design of SSA-based MPPT for PV-TEG hybrid system

4.1. MPPT design for PV-TEG model under PSC

The output voltages of both systems under specific weather conditions are considered optimization variables. The MPPT controller extracts the optimal duty ratio (Dc) associated with the best output voltage, which is fed into an insulated gate bipolar transistor (IGBT) for the next iteration. The fitness function for each control cycle can be determined through the collection of actual voltage and current readings, described by

$$\min f(V_{\mathrm{PV}}) = -P_{\mathrm{out}}(V_{\mathrm{PV}}) = -V_{\mathrm{PV}} * I_{\mathrm{PV}}(V_{\mathrm{PV}}) \tag{20}$$

$$\text{s. t. } V_{\mathrm{PV}}^{\min} \le V_{\mathrm{PV}} \le V_{\mathrm{PV}}^{\max} \tag{21}$$

where P_{out} stands for the active power generated by the entire PV array, and $V_{\mathrm{PV}}^{\min}$ and $V_{\mathrm{PV}}^{\min}$ denote the lower and upper limits of its output voltage, respectively.

The fitness function for TEG systems is similar to that for PV systems, as follows:

$$\min f(V_{\mathrm{TEG}}) = -P_{\mathrm{out}}(V_{\mathrm{TEG}}) = -V_{\mathrm{TEG}} * I_{\mathrm{TEG}}(V_{\mathrm{TEG}}) \tag{22}$$

$$\text{s. t. } V_{\mathrm{TEG}}^{\min} \le V_{\mathrm{TEG}} \le V_{\mathrm{TEG}}^{\max} \tag{23}$$

where P_{out} represents the active power of the whole TEG system, and $V_{\mathrm{TEG}}^{\min}$ and $V_{\mathrm{TEG}}^{\max}$ are the lower and upper limits of the output voltage of TEG system, respectively.

4.2 Boost converter model

Boost circuit is a non-isolated DC-DC converter that raises input voltage, which is widely used as MPPT technique in two-stage PV and TEG systems due to its simple structure and high conversion efficiency [32]. Specifically, Figure 6 displays the SSA-based MPPT model of PV-TEG array under PSC via boost converter.

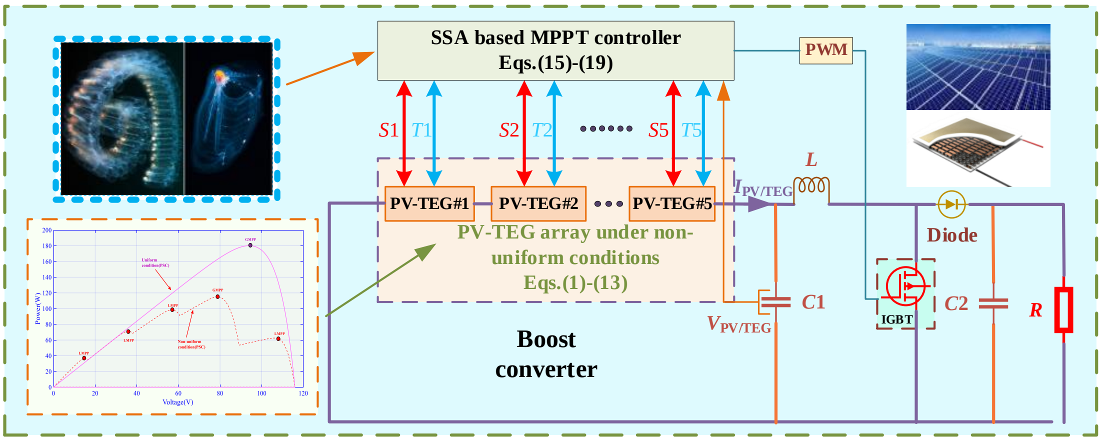

Fig. 6. Illustrative representation of MPPT design for PV-TEG hybrid system under PSC via SSA.

As shown in Fig. 6, $V_{PV/TEG}$ represents the output voltage of the PV/TEG array. V_{out} denotes the output voltage of the boost circuit. Besides, f and T mean the switching frequency of IGBT and control cycle, respectively. I_L and I_{Lmax} stand for the rated current and peak current the inductor L, individually. The calculation method for V_{out}, L, and filter capacitance C_1 can be explained as follows

$$V_{\mathrm{out}} = \frac{V_{\mathrm{PV/TEG}}}{1-Dc} \tag{24}$$

$$L = \frac{V_{\mathrm{out}}}{4I_{\mathrm{pmax}} \times f} \tag{25}$$

$$C_1 = L \times \frac{(I+I_{\mathrm{pmax}}/2)^2-(I-I_{\mathrm{pmax}}/2)^2}{(V_{\mathrm{in}}+0.005V_{\mathrm{in}})^2-(V_{\mathrm{in}}-0.005V_{\mathrm{in}})^2} \tag{26}$$

Note that the filter capacitor is designed to reduce the impact of ripple current generated by the inductor on the PV system. In particular, the settings of boost circuit parameters for two subsystems in PV-TEG hybrid system are shown in Table 2. Generally speaking, DC-DC converters have losses, the tracking efficiency of the MPPT technology can be defined as

$$\eta_{\mathrm{MPPT}} = \frac{P_{\mathrm{PV-TEG}}(t)}{P_{\max}(t)} \times 100 \tag{27}$$

where $P_{\text{PV-TEG}}(t)$ and represent the actual power and the maximum power obtained by the hybrid system at time t, respectively.

Table 2. Parameter setting of boost circuit.

parameter	PV system	TEG system
Capacitor	C_1=C_2=1 μF	C_1=66 μF, C_2=200 μF
Inductor(L)	500 mH	250 mH
Resistive load(R)	200 Ω	10 Ω
Switching frequency	100 kHz	f_s=20 kHz

4.3 Overall execution procedure

MPPT of PV-TEG hybrid system combines the individual techniques of both subsystems. The proposed non-model-based MPPT technique gathers two parameters, namely voltage and current, requiring identical MPPT controllers for PV and TEG subsystems. Thus, the overall MPPT execution process for both systems is similar, as illustrated in Fig. 7, upon which a parallel optimization process are conducted.

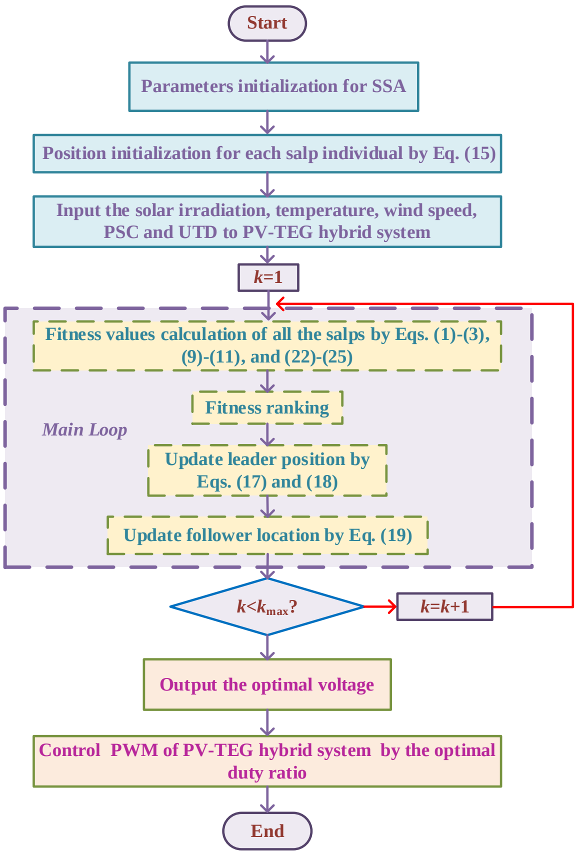

Fig. 7. Overall optimization process of SSA-based MPPT for PV-TEG hybrid system under PSC.

5. Case Study

To comprehensively evaluate the optimization performance of SSA-based MPPT controllers for PV-TEG hybrid systems affected by both PSC and NTD, this section establishes four testing cases: (a) start-up testing, (b) stepwise variations in solar irradiation at constant temperature, (c) stochastic change in solar irradiation, and (d) field measured data of temperature and solar radiation for typical days in Hong Kong. In addition, two traditional methods and ten heuristic algorithms are used as comparison methods, i.e., INC and P&O, as well as moth-flame optimization algorithm (MFO) [33], dragonfly algorithm (DA) [34], mud ring algorithm (MRA) [35], grey wolf optimization algorithm (GWO) [36], reptile search algorithm (RSA) [37], arithmetic trigonometric optimization algorithm (ATO) [38], firefly algorithm (FA) [39], whale optimization algorithm (WOA) [40], arithmetic optimization algorithm [22], and atomic orbital search (AOS) [23]. Note that for MhAs, population size N_p and maximum iteration number k_{max} are decisive parameters for optimization processes, which are uniformly set to 12 and 5, respectively, for fair comparations. The step sizes of INC and P&O are set to 10^{-6}. Moreover, table 3 provides detailed parameter settings for PV-TEG hybrid system. The optimal parameters for all compared methods have been rigorously tested and validated through extensive experimentation processes, ensuring solution's quality and calculation speed. Specifically, Fig. 8 shows MPPT model of SSA-based PV-TEG hybrid system implemented by Matlab/Simulink, in which the scale of both PV subsystem and TEG subsystem is 5×1 and DC-DC circuit selects a boost converter.

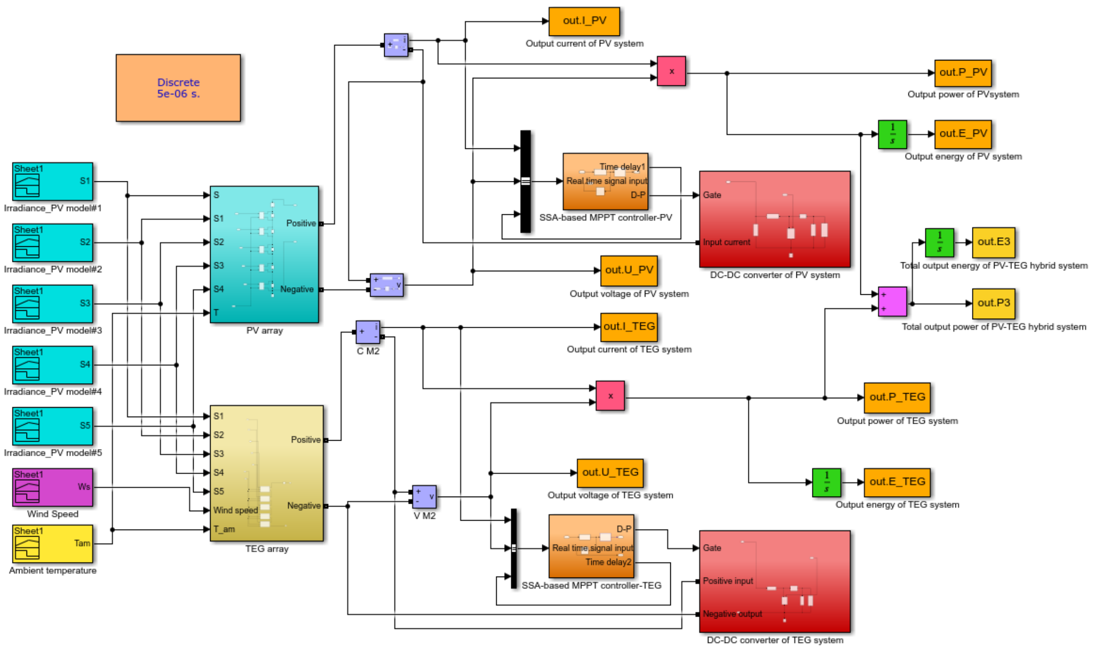

Fig. 8. Model of PV-TEG hybrid system implemented through Matlab/Simulink.

Furthermore, all trials are carried out utilizing the advanced MATLAB/Simulink 2022a platform, employing an Ode 45 solver with adaptive step sizes. The computations are executed on a high-performance personal computer, equipped with an Intel Core TMi9 CPU, boasting a processing speed of 3.0 GHz, and a colossal 128 GB of RAM. In addition, to more intuitively evaluate the optimization results of various methods for PV-TEG hybrid systems, two indicators are introduced to calculate power fluctuations, as follows [41]

$$\Delta v^{\mathrm{avg}} = \frac{1}{T-1}\sum_{t=2}^{T}\frac{|P_{\mathrm{out}}(t)-P_{\mathrm{out}}(t-1)|}{P_{\mathrm{out}}^{\mathrm{avg}}} \tag{28}$$

$$\Delta v^{\max} = \max_{t=2,3,\cdots,T}\frac{|P_{\mathrm{out}}(t)-P_{\mathrm{out}}(t-1)|}{P_{\mathrm{out}}^{\mathrm{avg}}} \tag{29}$$

where elucidations for all aforementioned variables can be found in reference [41].

Table 3. Component parameters of PV-TEG hybrid system.

PV module		TEG module	
Type	User-defined	Type	TGM199-1.4-2.0
Typical peak power	51.716 W	Parameter measurement conditions	T_c=30 °C, T_h=200 °C
Mpp Voltage	18.47 V	Component dimensions	40 mm×40 mm×4.4 mm
Mpp current	2.8 A	Typical peak power	7.3 W
Short-circuit current(I_{sc})	1.5 A	I_{sc}	2.65 A
Open-circuit voltage(V_{oc})	23.36 V	V_{oc}	11 V
Temperature coefficient of Isc(k_1)	3 mA/°C	Number of thermoelectric units	199

5.1 Start-up test

This assessment aims to verify the response speed and convergence stability of the SSA-based MPPT method during start-up. To accurately investigate PSC and NTD effect on PV-TEG, this test varies the solar irradiance across five PV modules (700 W/m^2, 200 W/m^2, 900 W/m^2, 600 W/m^2, and 500 W/m^2) while keeping the temperature constant at 25°C. The hot side input temperatures of TEG modules is calculated using Eq. (12), while their cold side temperatures remain fixed at 25°C.

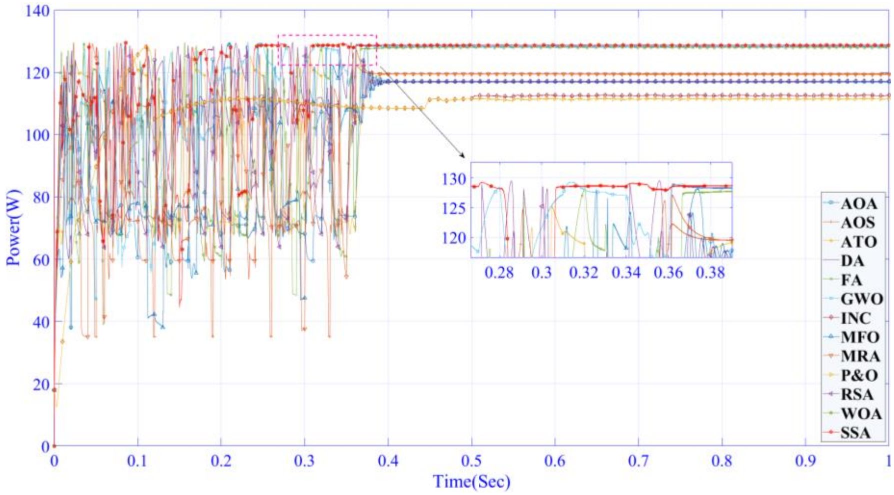

(a)

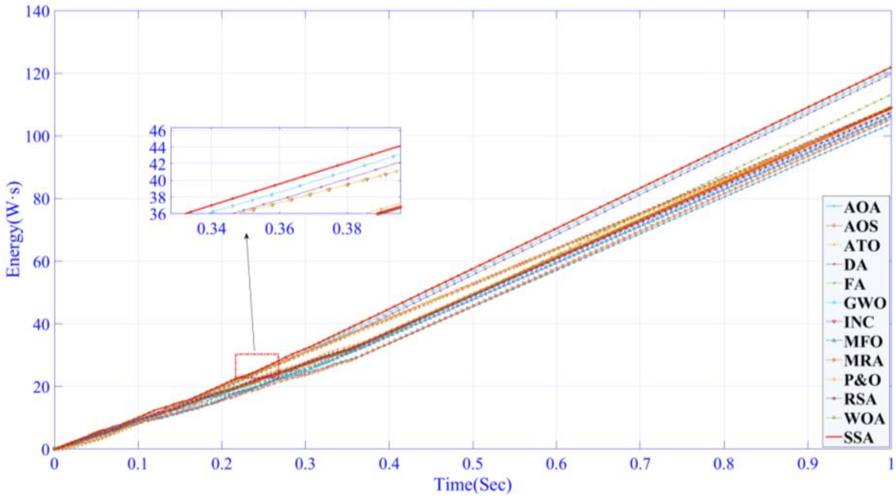

(b)

Fig. 9. Performance on the start-up test via thirteen methods evaluated by PV-TEG hybrid system. (a)Power obtained by PV-TEG hybrid system and (b) Energy obtained by PV-TEG hybrid system.

Figure A1 in appendix shows the *P*-*V* and *I*-*V* curves of PV subsystem and TEG subsystem. The *P*-*V* curve of PV system has multiple peaks, while *P*-*V* curve of TEG system has only a single peak, which makes the MPPT difficulty of PV system higher than that of TEG system. Figure 9 illustrates online optimization outcomes acquired from thirteen distinct MPPT strategies, upon which INC and P&O not only have slow convergence speed and large power fluctuations (ΔV^{avg} and ΔV^{max}) but also fall into low-quality LMPP, while MhAs can converge to more excellent power points in a relatively short time. Additionally, as shown in Fig. 9 (a), compared to the other ten MhAs and two traditional mathematical methods, SSA has the fastest convergence speed, the highest quality solution, and the shortest oscillation time thanks to its excellent global search mechanism. Moreover, the current, voltage, and obtained power of PV and TEG subsystems are shown in Fig. A2 in appendix.

Table 5 shows the optimization results of each method under the start-up test. SSA generated 121.93 W of power, which is 15.67%, 17.44%, and 11.88% higher than that of MRA, AOA, and AOS, respectively. Simultaneously, SSA exhibits minimal power fluctuations, with an average variable rate almost one-third smaller than MRA, and a maximum variation rate almost five times smaller than MRA.

5.2 Stepwise variations in solar irradiation at constant temperature

This section aims to simulate how the rapid movement of clouds affects the power output of the PV-TEG array at a constant temperature of 25°C. Figure 10 shows that each PV panel receives solar radiation with a different step change, leading to different input temperatures at the hot side of each TEG module according to Eq. (12).

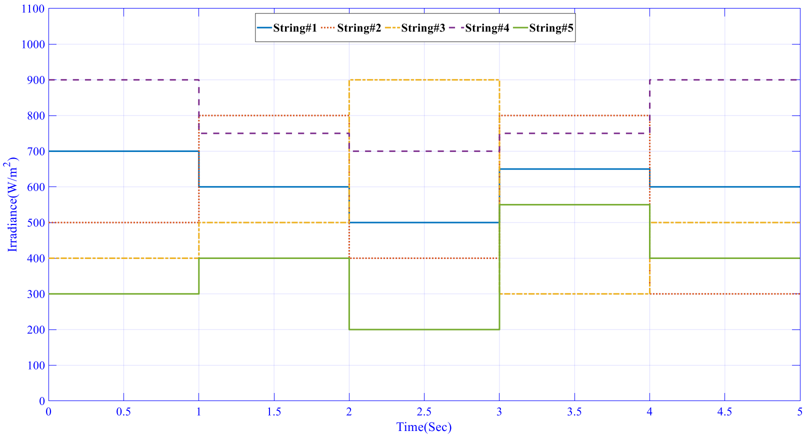

Fig.10. Step changed solar irradiation under PSC.

Figure A3 in appendix shows the electrical characteristic curves of PV subsystem and TEG subsystem in five stages. Due to the small temperature difference of TEG module, the *P*-*V* characteristic curve of TEG system is relatively smooth. The online optimization results of each method under step illumination conditions are presented in Fig. 11. Notably, Fig. 11 (a) illustrates that SSA has the fastest convergence rate among all methods, while Fig. 11 (b) shows that SSA generates the highest energy of 562.29 W·s. Additionally, solar irradiance increases power fluctuations of INC and P&O during step changes, while MhAs greatly avoid this transient process. Moreover, the current, voltage, and obtained power of PV and TEG subsystems are shown in Fig. A4 in appendix. Importantly, SSA obtains the smallest power variation rate (ΔV^{avg} and ΔV^{max}), confirming the powerful stability of SSA-based MPPT for PV-TEG system under step input conditions.

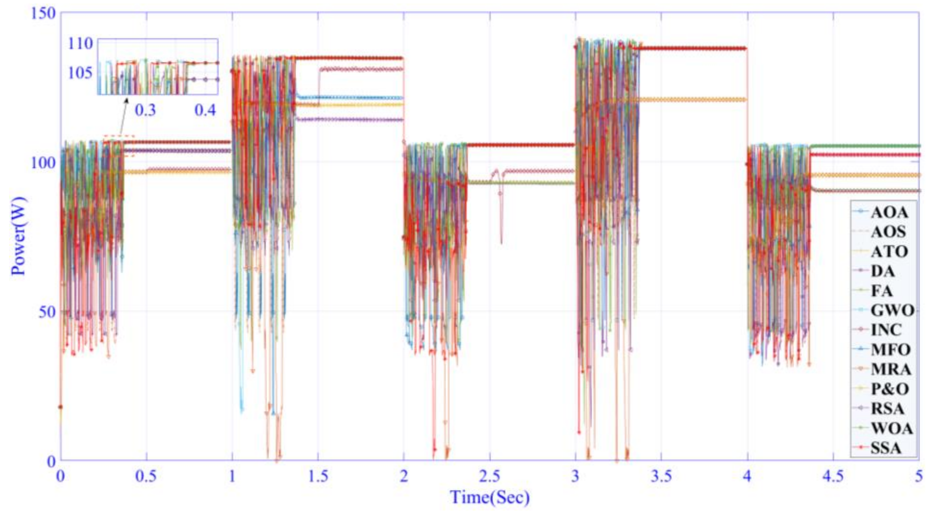

(e)

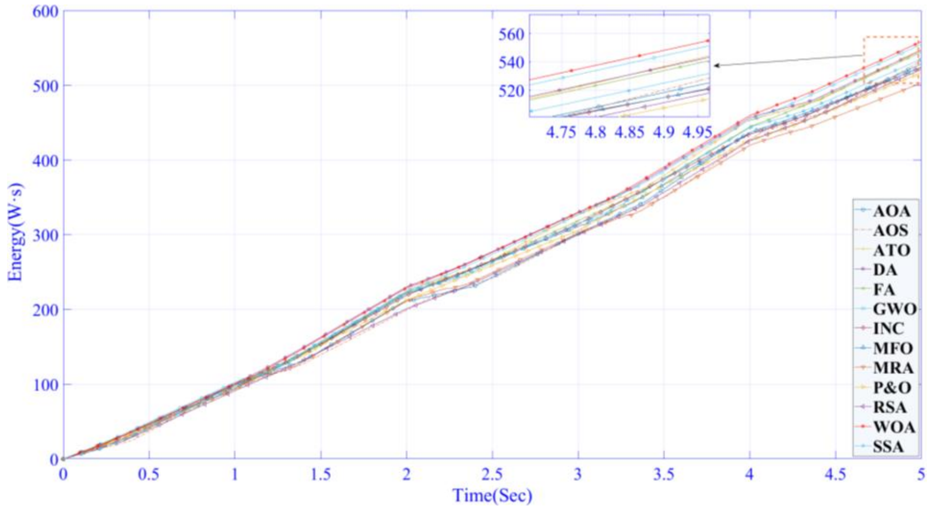

(f)

Fig. 11. Results of PV-TEG hybrid system under step change with constant temperature via thirteen methods. (a) Power obtained by PV-TEG hybrid system and (b)Energy obtained by PV-TEG hybrid system.

5.3 Stochastic change in solar irradiation

To simulate typical summer day conditions with a duration of 12 daytime hours, this section implements continuous and random changes to irradiance conditions, as illustrated in Fig. 12. The thermal change at the hot side of the TEG module is also subjected to continuous and random variations for 12 hours, while the cold side temperature remains constant at 25°C.

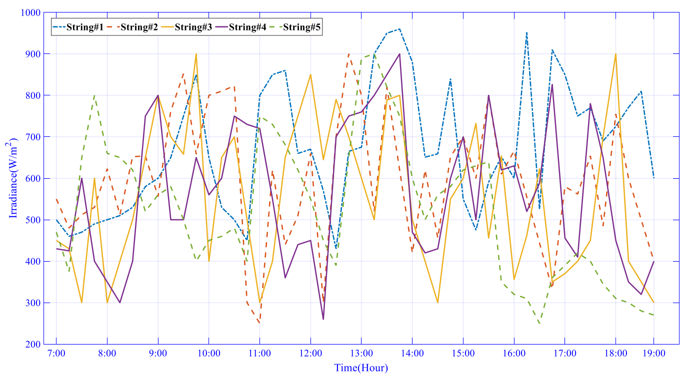

Fig. 12. Stochastic irradiance change of PV-TEG hybrid system

Figure 13 depicts the MPPT results of PV-TEG hybrid system obtained by thirteen methods under the stochastic change in solar irradiation. Particularly, Fig. 13 (c) highlights that SSA yields the highest energy output, surpassing P&O, AOA, AOS by 21.82%, 13.92%, and 13.38%, respectively, which suggests that SSA is capable of achieving superior power output, despite the long-term, continuous, and random variations in irradiance conditions resulting in slight power fluctuations.

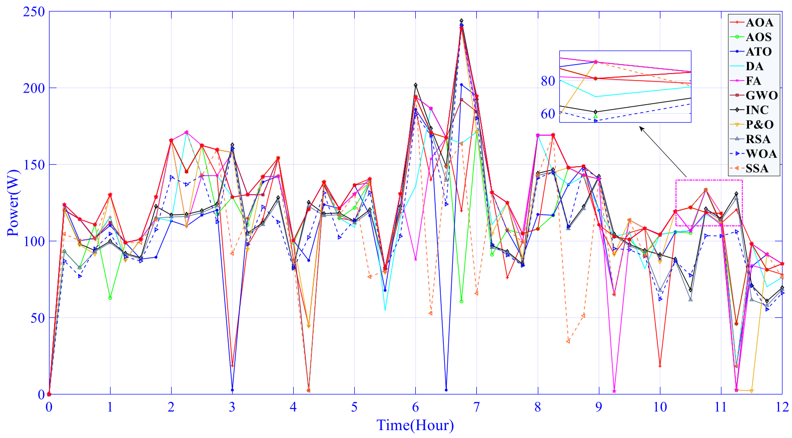

(a)

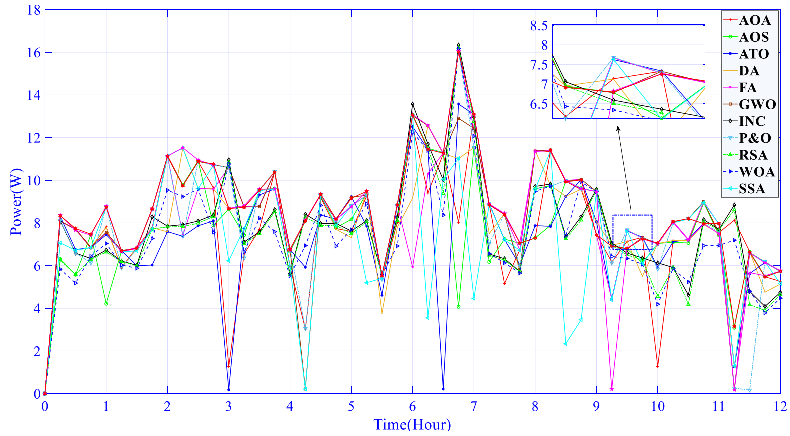

(b)

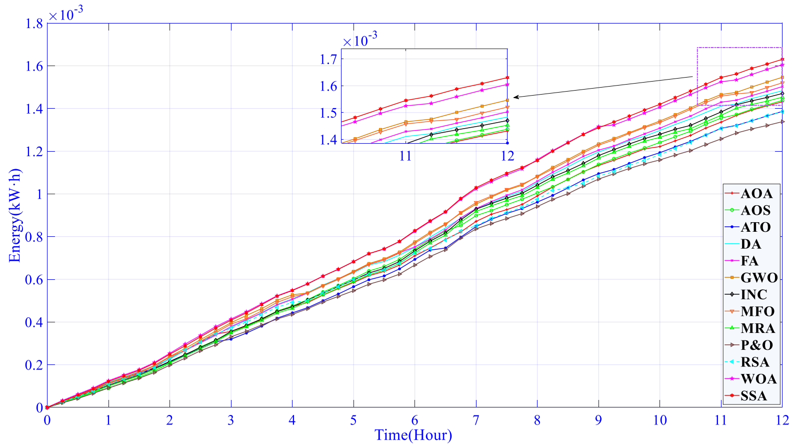

(c)

Fig. 13. PV-TEG hybrid system responses of thirteen methods obtained on stochastic irradiance. (a)Power obtained by PV-TEG hybrid system, (b) Power obtained by TEG subsystem, and (c)Energy obtained by PV-TEG hybrid system.

5.4 Field measured data of temperature and solar radiation for typical days in Hong Kong

Thirteen different methods are assessed using solar irradiance and temperature measurements from Hong Kong, a subtropical region situated in the eastern Pearl River Estuary of China. Hong Kong's climate is classified as a subtropical monsoon climate, characterized by hot and rainy summers, with temperatures ranging from approximately 27 °C to 33 °C, and cool and dry winters, with an average annual temperature of 22.8 °C. Typhoons, which are often generated by tropical cyclones in the western North Pacific and East China Sea, frequently affect Hong Kong from July to September. The data for this study were collected from four typical days during each of the four seasons in 2022, with a ten-minute sampling interval. The sampling location is shown in Fig. 14 (a), situated at 22.3° north latitude and 114.2° east longitude. The specific measurement instruments (JD-WG-CQD) used in this study are depicted in Fig. 14 (b), which is a small meteorological station that can remotely view data in real-time through cloud platforms, including temperature, humidity, lighting, atmospheric pressure, and wind speed sensors. The types of sensors can be selected by users within a certain range, additionally, the parameters of the measuring equipment are shown in Table 4. Unlike the random and continuous variation of solar irradiance in section 5.3, this section assumes uniform lighting conditions for all PV panels, which represents long-term, continuous step changes. Additionally, TEG modules are found to exhibit no NTD based on Eq. (12).

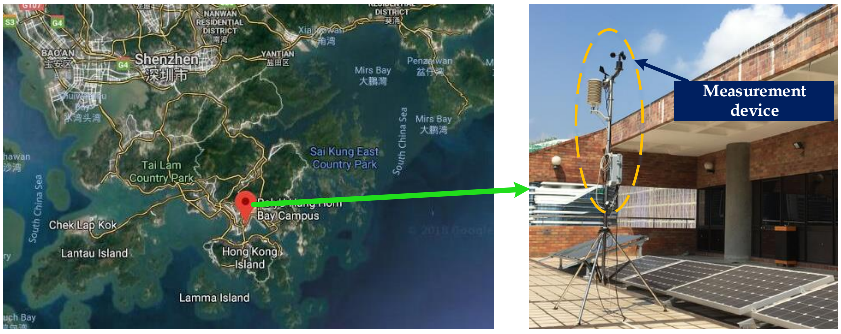

(a) (b)

Fig. 14. Detailed geographical location of solar radiation and temperature measurement devices.

Table 4. Equipment parameters of small meteorological stations.

Measured data	Measuring range	Measured data	Measuring range
Wind speed	0-70m/s	Irradiance	0-100Klx(±0.3%)
Wind direction	0-360°(±1°)	Optical rainfall	0-4mm/min(±4%)
Atmospheric pressure	300hPa-1100hPa(±0.25%)	Sunshine recorder	Support with a height of 60cm
Temperature	-40°C-85°C(±0.3°C)	Data storage	Not less than 500000 pieces
Air humidity	0-100%RH(±0.25%)	Consumption	1.75W

Figure 15 (a) displays the measured lighting data for four typical days in Hong Kong, and Fig. 15 (b) shows TEG cold side temperature set to measured ambient temperature.

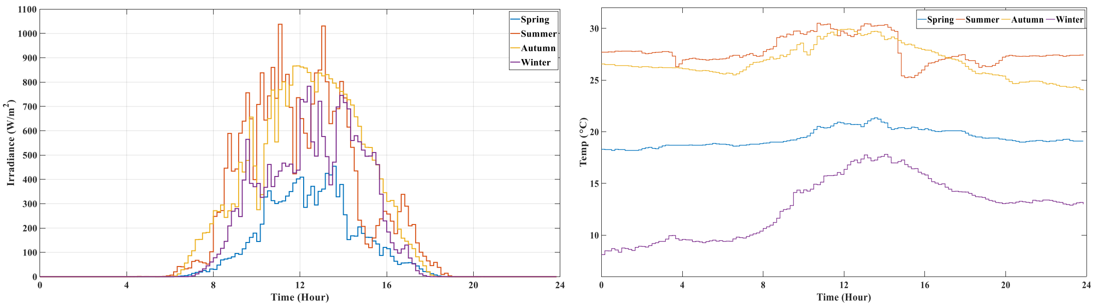

(a) (b)

Fig. 15. Measured atmospheric data on typical days in Hong Kong. (a) Solar irradiation and (b) Temperature.

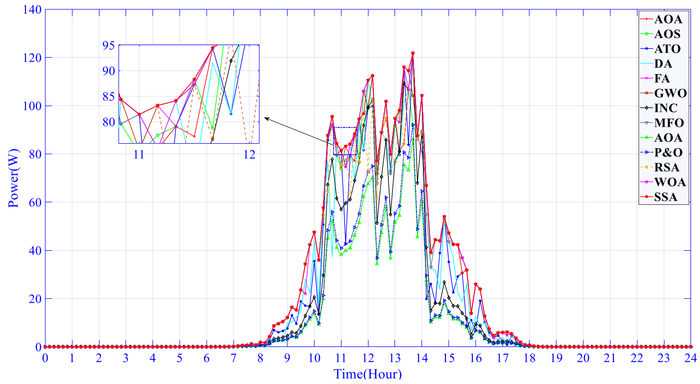

(a)

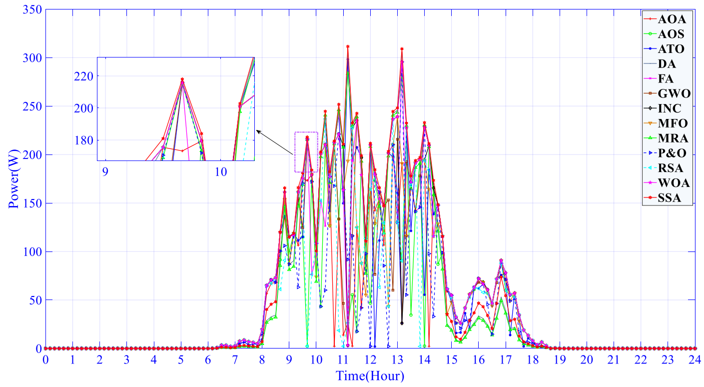

(b)

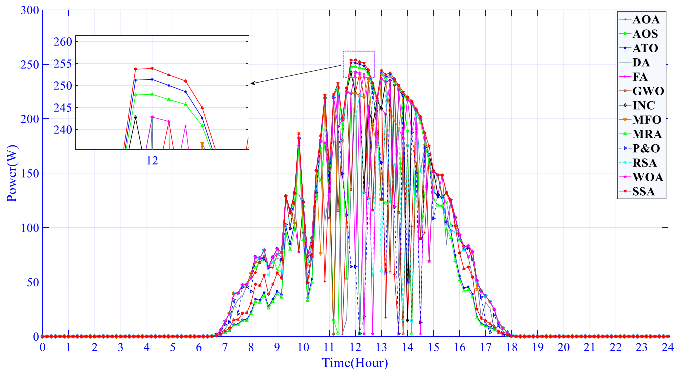

(c)

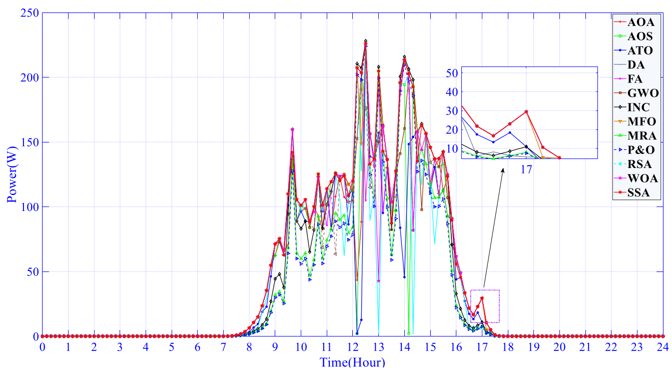

(d)

Fig. 16. Power obtained by PV-TEG hybrid system on different typical days via thirteen methods. (a) Spring (b) Summer, (c) Autumn, and (d) Winter.

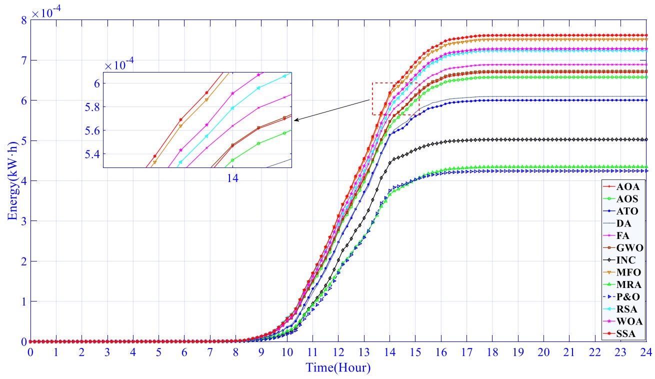

(a)

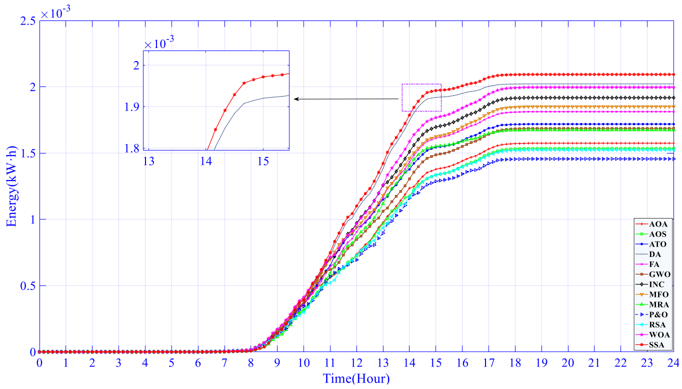

(b)

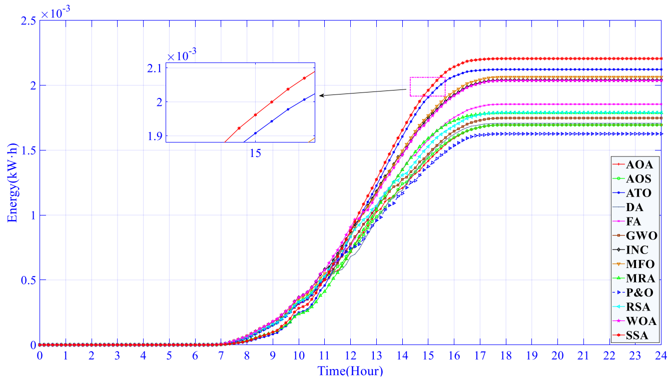

(c)

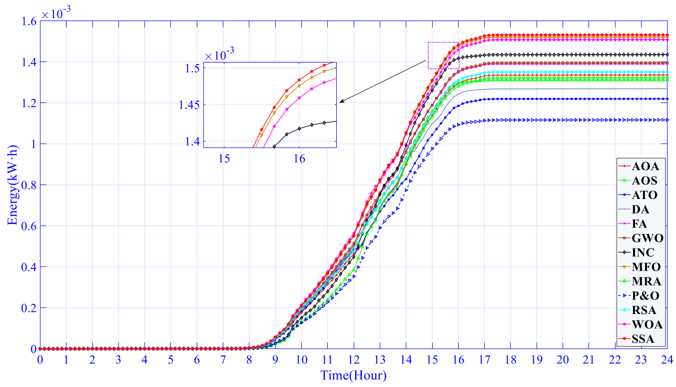

(d)

Fig. 17. Energy obtained by PV-TEG hybrid system on different typical days via thirteen methods. (a) Spring (b) Summer, (c) Autumn, and (d) Winter.

Figures 16, A5, A6, 17, A7, and A8 show optimal outcomes (i.e. Obtained power in PV-TEG hybrid system, PV subsystem, and TEG subsystem, respectively, obtained energy in PV-TEG hybrid system, PV subsystem, and TEG subsystem, respectively.) for thirteen methods under Hong Kong measurement data input conditions. It can be seen that MhAs can obtain higher energy with smaller power fluctuations (ΔV^{avg} and ΔV^{max}) than INC and P&O in most cases. Inspiringly, SSA achieves the highest energy in four typical seasonal days and acquires the smallest power fluctuations (ΔV^{avg} and ΔV^{max}) on typical winter days. Under long-term real data input conditions, although MhAs outperform INC and P&O, the optimization results obtained by each type of MhA vary greatly. In particular, SSA can always acquire the most outstanding and satisfactory optimization indexes on four typical days in four seasons, which verifies its significant stability and feasibility in practical engineering.

5.5 Energy conversion efficiency of TEG system

Considering the Seeback effect, Joule heat, Fourier heat conduction, and Thomson heat due to current and temperature gradients, the expression for the heat transferred from the back of the photovoltaic module to the TEG module is as follows [42]

$$Q_{\mathrm{h}} = \left(\alpha_{\mathrm{pn}} I_{\mathrm{TEG}} T_{\mathrm{h}} - \frac{I_{\mathrm{TEG}}^{2} R_{\mathrm{TEG}}}{2} + K_{\mathrm{TEG}}(T_{\mathrm{h}} - T_{\mathrm{c}}) - \frac{\mu T_{\mathrm{TEG}}(T_{\mathrm{h}} - T_{\mathrm{c}})}{2}\right) \tag{30}$$

where I_{TEG} is the current of the TEG module, R_{TEG} is the internal resistance of the TEG module, K_{TEG} is the thermal resistance of the TEG module, and μ is the Thomson coefficient.

Additionally, the thermal conductivity and Thomson coefficient of TEG are represented as follows [43]

$$k_{\mathrm{p}}=k_{\mathrm{n}}=(62605.0-277.7T_{\mathrm{av}}+0.4131T_{\mathrm{av}}^{2})\times10^{-4} \tag{31}$$

$$\mu=\mu_{\mathrm{p}}-(-\mu_{\mathrm{n}})=2\times(930.6T_{\mathrm{m}}-1.98T_{\mathrm{m}}^{2})\times10^{-9} \tag{32}$$

Moreover, the thermal resistance of the TEG module is represented as follows:

$$K_{\mathrm{TEG}} =\left(\frac{K_p A_p}{L_p} + \frac{K_n A_n}{L_n}\right)+K_{\mathrm{cm}} \tag{33}$$

where the explanations for all the variables mentioned above can be found in reference [43].

Conversion efficiency of TEG system η_{TEG} is defined as the ratio of the total output power generated by the TEG system to the total heat absorbed by the hot side, as follows

$$\eta_{\mathrm{TEG}} = \frac{\sum_{i=1}^{5} P_{\mathrm{TEG}i}}{\sum_{i=1}^{5} Q_{\mathrm{h}i}} \tag{34}$$

where $P_{\mathrm{TEG}i}$ and $Q_{\mathrm{h}i}$ represent the energy generated by the i-th TEG module and the heat absorbed by the hot side, respectively.

Due to the constant changes in the power and current of TEG during the optimization process of SSA, the efficiency values after power stabilization are given in start-up test and stepwise variations in solar irradiation at a constant temperature, and the average efficiency values are given in stochastically changing solar irradiation and field measured data in Hong Kong. Note that in Hong Kong measured data, only the time period with light input is selected for calculation. The energy conversion efficiency of the TEG system is 4.19% in start-up test, 4.14%, 4.59%, 4.00%, 4.23%, and 3.98% in five stages of stepwise variations in solar irradiation, respectively. The average efficiency is 4.19% in stochastically changing solar irradiation; In measured data in Hong Kong, the average efficiency is 4.07% in spring, 4.35% in summer, 4.24% in autumn, and 3.92% in winter.

5.6 Statistical results

Table 5 shows the statistical results of MPPT for PV-TEG hybrid system using thirteen methods under four scenarios, with optimal results displayed in bold. It is easy to see that SSA produces the highest energy in all scenarios, and exhibits the smallest power fluctuation (ΔV^{avg} and ΔV^{max}) in start-up testing, step irradiance change, and winter typical day scenarios measured in Hong Kong. During typical summer days in Hong Kong, energy yielded by SSA is 137.43%, 143.75%, 125.10%, 124.21%, 121.83% , 132.97%, and 135.03% of RSA, P&O, MRA, GWO, ATO, AOA, and AOS, respectively. Long periods and continuous time-varying input conditions further test the SSA optimization performance, especially under random irradiance changes and the case of measured data in Hong Kong. INC, P&O, and ten types of MhAs other than SSA may excessively converge to low-quality LMPP, resulting in higher power fluctuations (ΔV^{avg} and ΔV^{max}). This also proves that the excellent global optimization mechanism of SSA is more suitable for the complex MPPT process of PV-TEG hybrid systems.

6. Conclusions

Modern renewable energy systems are continually advancing towards hybrid power generation and control. Compared with traditional PV systems, PV-TEG hybrid systems can achieve more effective and cleaner electricity production. This study presents an SSA-based MPPT technique for optimizing the performance of PV-TEG hybrid systems under various PSCs. Its main contributions and innovative aspects are summarized as follows:

(1) This study proposes a PV-TEG hybrid power generation strategy to address the limitations of PV and TEG systems, thus enhancing power generation efficiency;

(2) Due to a concise, stable, and efficient optimization mechanism, SSA is capable of acquiring more energy and minimal power fluctuation (ΔV^{avg} and ΔV^{max}) at a faster rate than traditional methods, including INC and P&O, as well as ten advanced MhAs such as AOA, AOS, DA, ATO, RSA, MRA, FA, WOA, GWO and MFO;

(3) To further validate the advantages of SSA, three comprehensive and profound case studies are conducted, i.e., start-up tests, stepwise variations in solar irradiation at a constant temperature, and stochastically changing solar irradiation. Besides, Hong Kong's field atmospheric data are used as the fourth evaluation case to realistically verify SSA's response performance in PV-TEG hybrid systems.

(4) SSA exhibited superior performance in all tests. Particularly, by executing SSA-based MPPT strategies, an additional 12.04% and 11.56% of energy are generated under start-up testing and stepwise variations in solar irradiation at a constant temperature, respectively.

To enhance future research, two key aspects should be prioritized:

(1) Developing a lossless electrical connection for PV-TEG hybrid modules to build a centralized PV-TEG array or implementing a physically connected PV-TEG hybrid system with a dual input high gain boost circuit to improve energy production efficiency while reducing manufacturing and operational costs;

(2) Employing SSA-based MPPT controllers for larger-scale PV-TEG hybrid systems and establishing a large-scale grid-connected power supply system for PV-TEG.

Acknowledgments

This work was supported by National Natural Science Foundation of China (61963020, 62263014) and Yunnan Provincial Basic Research Project (202201AT070857).

Table 5. Comparison of statistical inference across four testing scenarios via thirteen techniques in PV-TEG hybrid system.

Scenes		Indices	AOA	AOS	ATO	DA	FA	GWO	INC	MFO	MRA	P&O	RSA	WOA	SSA
Start-up		Energy(W·s)	103.82	108.98	109.37	119.53	113.24	120.72	108.90	106.32	105.41	108.35	107.51	121.92	**121.93**
		ΔV^{max}(%)	0.0246	0.0213	0.0375	0.0182	0.0189	0.0160	0.0307	0.0152	0.0658	0.0236	0.1056	0.0196	**0.0137**
		ΔV^{avg}(%)	0.0055	0.0052	0.0049	0.0043	0.0044	0.0043	0.0048	0.0043	0.0047	0.0050	0.0065	0.0042	**0.0041**
Stepwise variations in solar irradiation at constant temperature		Energy(W·s)	528.55	532.81	548.05	546.63	544.24	554.83	524.34	523.78	502.96	517.01	521.38	558.51	**562.29**
		ΔV^{max}(%)	42.89	40.93	45.01	42.41	40.96	41.13	54.22	41.42	44.66	58.73	42.57	40.36	**39.21**
		ΔV^{avg}(%)	0.0091	0.0087	0.0102	0.0089	0.0084	0.0086	0.0216	0.0091	0.0098	0.0312	0.0094	0.0088	**0.0079**
Stochastic change solar irradiation		Energy(10^{-6}kW·h)	143.13	143.81	138.65	148.35	150.29	154.64	147.03	152.04	145.31	133.84	138.47	160.51	**163.05**
		ΔV^{max}(%)	96.31	89.49	142.37	**65.93**	67.85	57.95	78.42	61.14	80.40	85.14	96.21	85.54	79.28
		ΔV^{avg}(%)	20.34	19.75	23.79	18.87	19.85	**16.56**	19.67	21.30	20.22	19.60	28.74	18.68	19.24
Field measured data of temperature and solar radiation for typical days in Hong Kong	Spring	Energy(10^{-6}kW·h)	6.694	6.578	6.002	6.099	6.887	6.727	5.025	7.514	4.343	4.243	7.236	7.279	**7.618**
		ΔV^{max}(%)	229.96	212.43	399.10	269.52	**171.06**	209.08	379.43	231.79	304.69	403.04	208.16	215.49	190.01
		ΔV^{avg}(%)	24.74	22.37	28.98	28.79	**16.61**	18.44	26.13	20.18	23.55	26.56	22.96	18.25	17.57
	Summer	Energy(10^{-6}kW·h)	15.74	15.35	17.18	20.22	18.12	16.85	19.17	18.25	16.73	14.56	15.23	19.96	**20.93**
		ΔV^{max}(%)	267.14	246.65	372.59	247.27	280.27	237.90	344.05	246.51	226.95	473.79	376.05	223.30	**215.72**
		ΔV^{avg}(%)	33.42	32.10	40.46	29.01	27.89	35.67	26.47	25.99	**14.55**	45.79	39.43	25.53	27.25
	Autumn	Energy(10^{-6}kW·h)	16.95	16.94	21.22	17.07	18.54	17.48	20.41	20.63	17.87	16.26	17.90	20.36	**22.06**
		ΔV^{max}(%)	256.95	233.36	**160.52**	376.19	308.28	259.19	344.05	289.03	154.90	337.01	313.96	361.50	215.72
		ΔV^{avg}(%)	27.79	24.43	14.84	36.40	24.85	35.67	22.00	17.62	14.55	36.61	31.44	25.80	**14.09**
	Winter	Energy(kW·h)	13.36	13.22	12.20	12.69	13.90	13.96	14.35	15.20	13.11	11.17	13.51	15.08	**15.32**
		ΔV^{max}(%)	276.55	254.84	497.06	485.61	214.53	144.38	302.35	216.07	369.99	315.08	249.53	187.02	**205.13**
		ΔV^{avg}(%)	29.88	26.35	29.73	36.41	23.87	19.43	24.29	19.24	27.23	23.69	24.26	19.47	**18.76**

Appendix

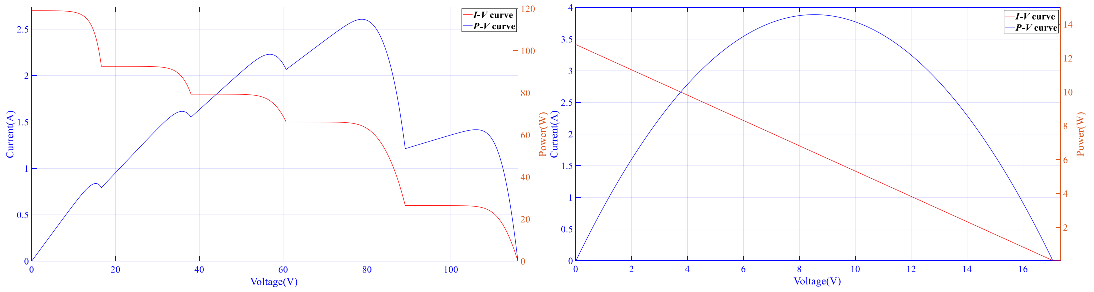

(a) (b)

Fig. A1. Electrical characteristic curve of PV-TEG hybrid system in start-up test. (a) *P-V* and *I-V* characteristic curves of PV subsystem and (b) *P-V* and *I-V* characteristic curves of TEG subsystem.

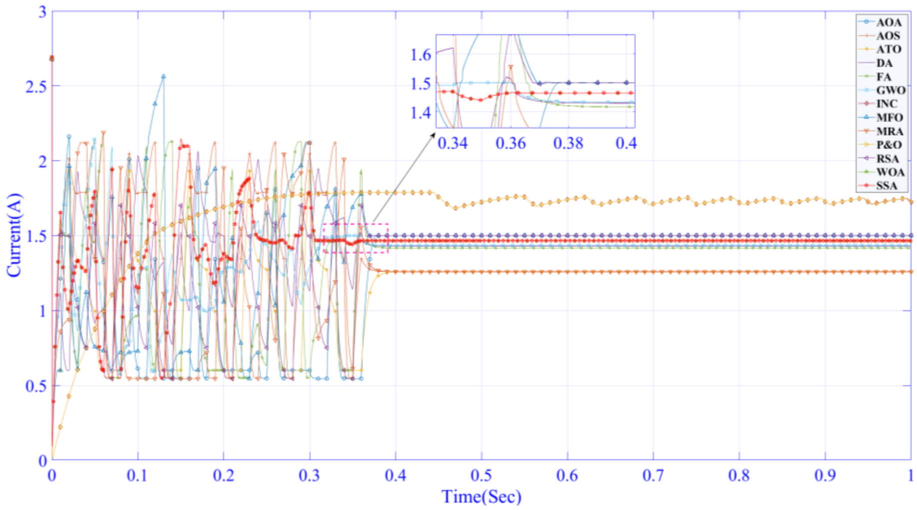

(a)

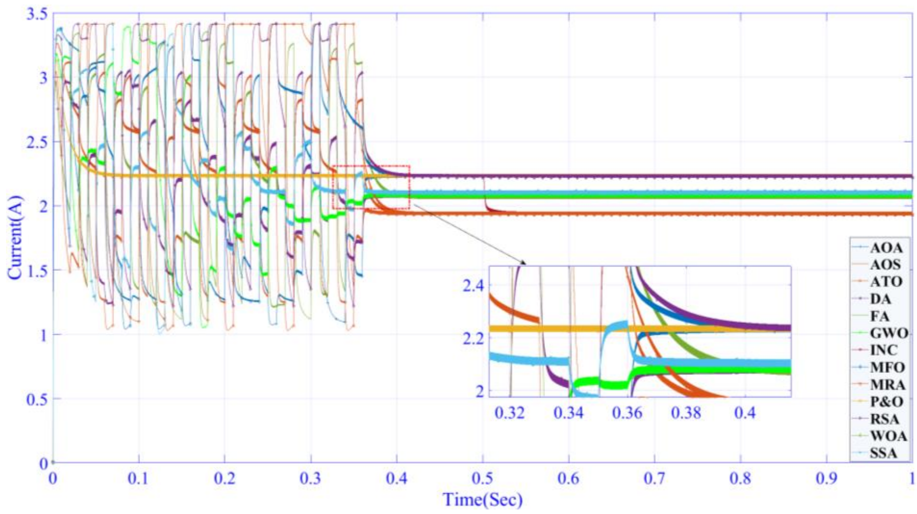

(b)

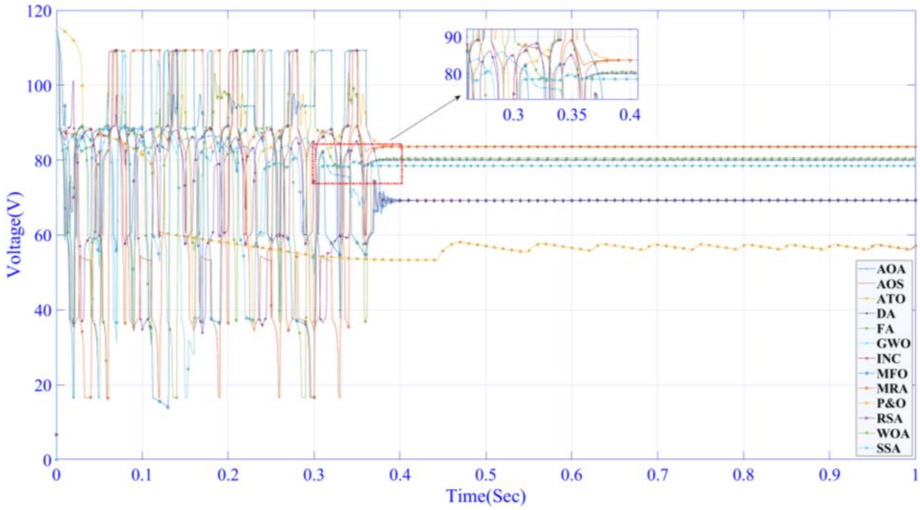

(c)

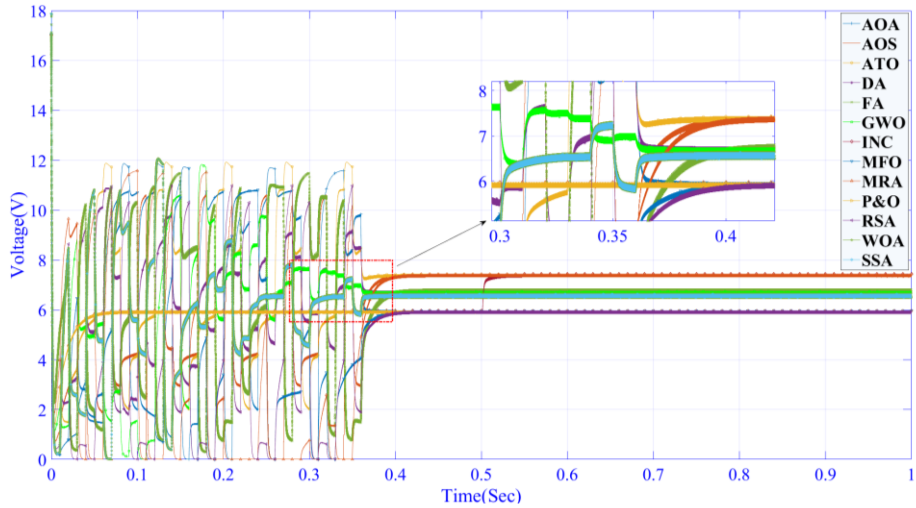

(d)

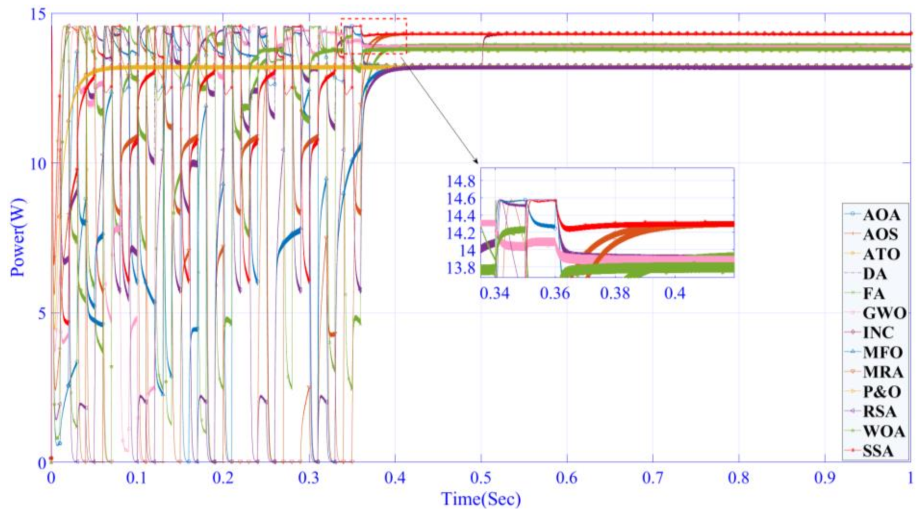

(e)

Fig. A2. Performance on the start-up test via thirteen methods evaluated by PV and TEG subsystems. (a) Current of PV system; (b) Current of TEG system; (c) Voltage of PV system; (d) Voltage of TEG system and (e) Energy obtained by TEG subsystem.

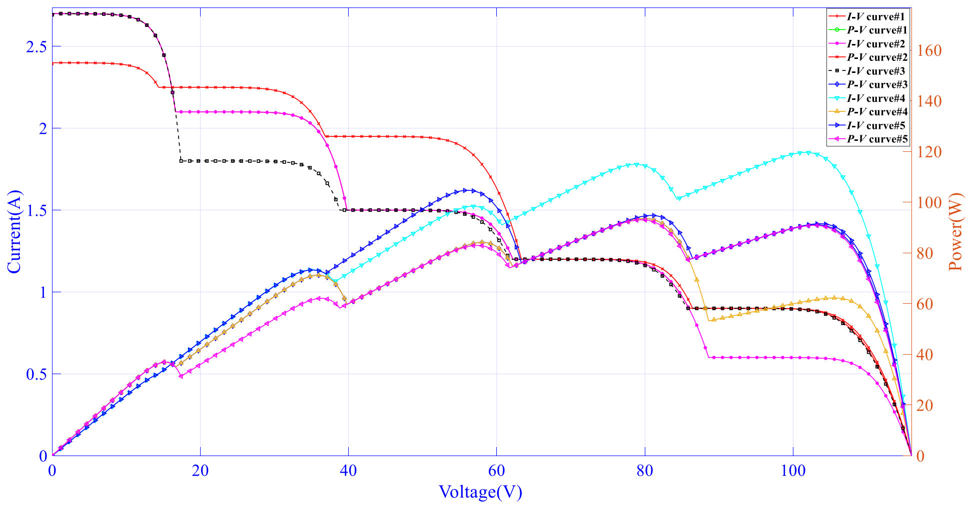

(a)

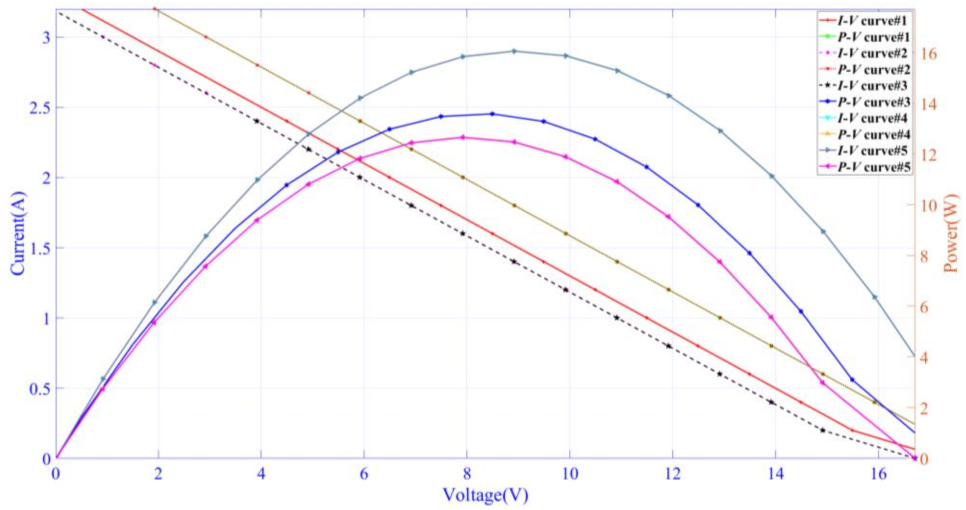

(b)

Fig. A3. Electrical characteristic curve of PV-TEG hybrid system in stepwise variations in solar irradiation at constant temperature. (a) *P-V* and *I-V* characteristic curves of PV subsystem and (b) *P-V* and *I-V* characteristic curves of TEG subsystem.

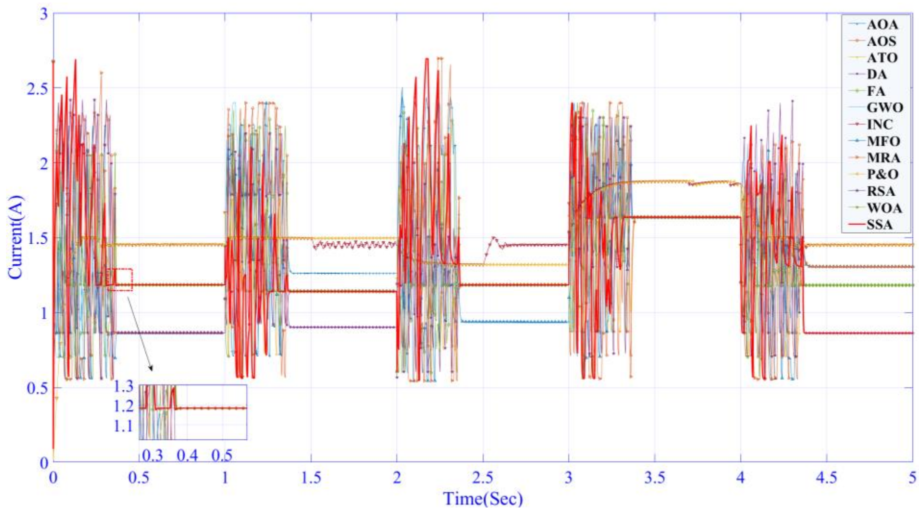

(a)

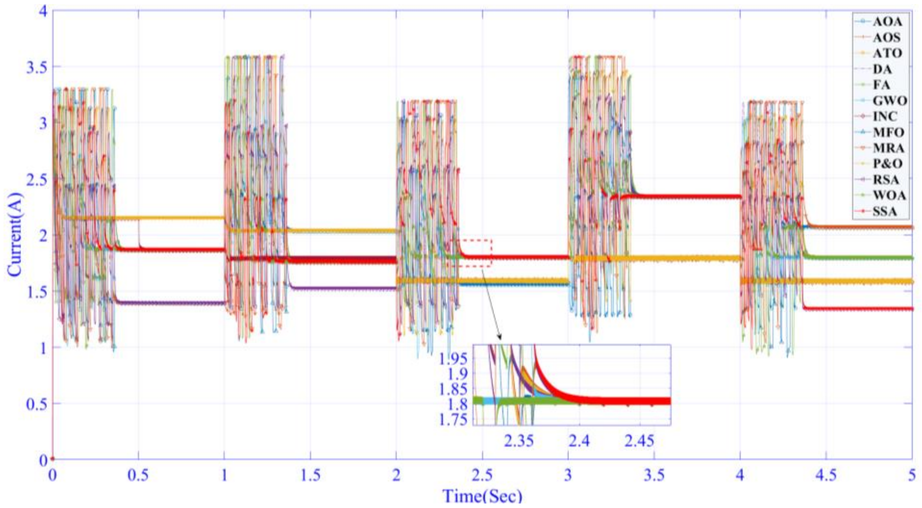
Current(A)
Time(Sec)
AOA
AOS
ATO
DA
FA
GWO
INC
MFO
MRA
P&O
RSA
WOA
SSA

(b)

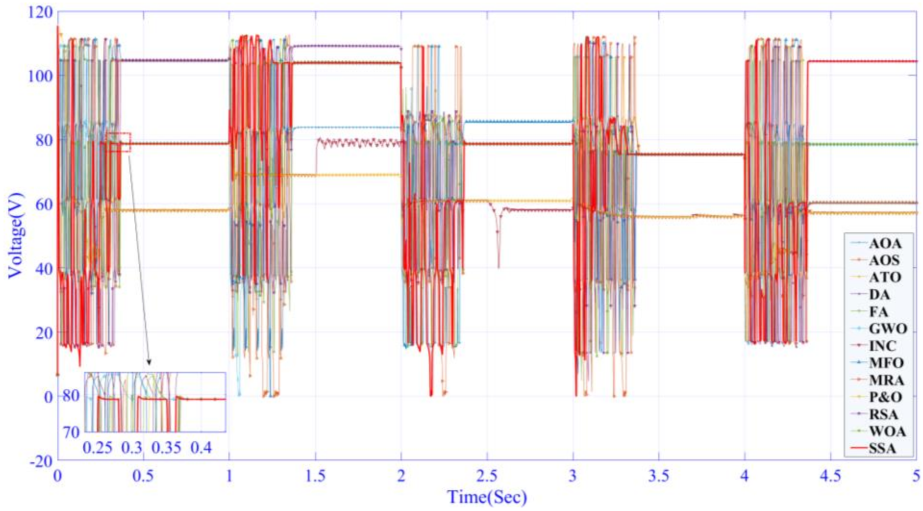
Voltage(V)
Time(Sec)
AOA
AOS
ATO
DA
FA
GWO
INC
MFO
MRA
P&O
RSA
WOA
SSA

(c)

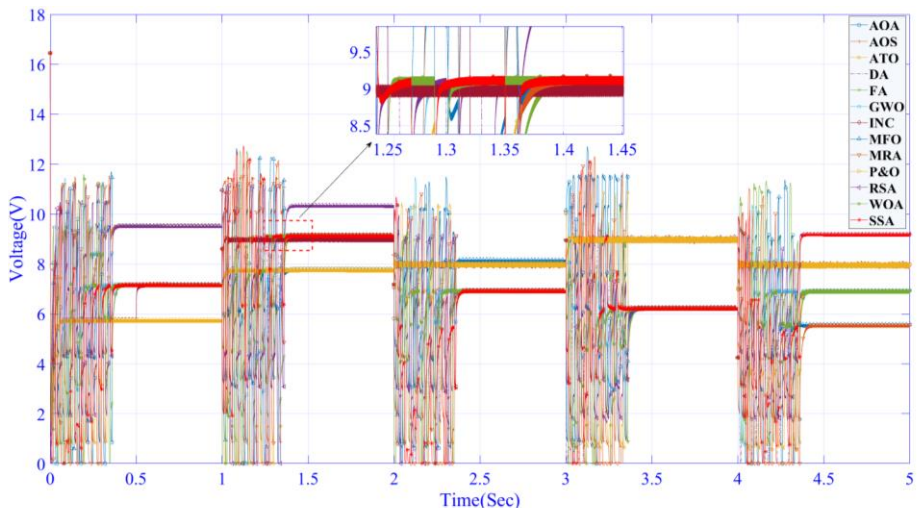
Voltage(V)
Time(Sec)
AOA
AOS
ATO
DA
FA
GWO
INC
MFO
MRA
P&O
RSA
WOA
SSA

(d)

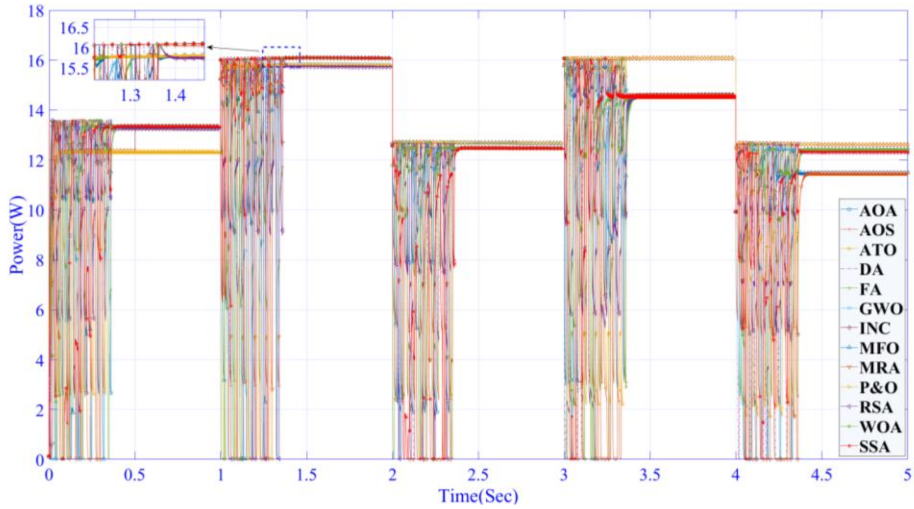

(e)

Fig. A4. Performance on the stepwise variations in solar irradiation at constant temperature via thirteen methods evaluated by PV and TEG subsystems. (a) Current of PV system; (b) Current of TEG system; (c) Voltage of PV system; (d) Voltage of TEG system and (e) Energy obtained by TEG subsystem.

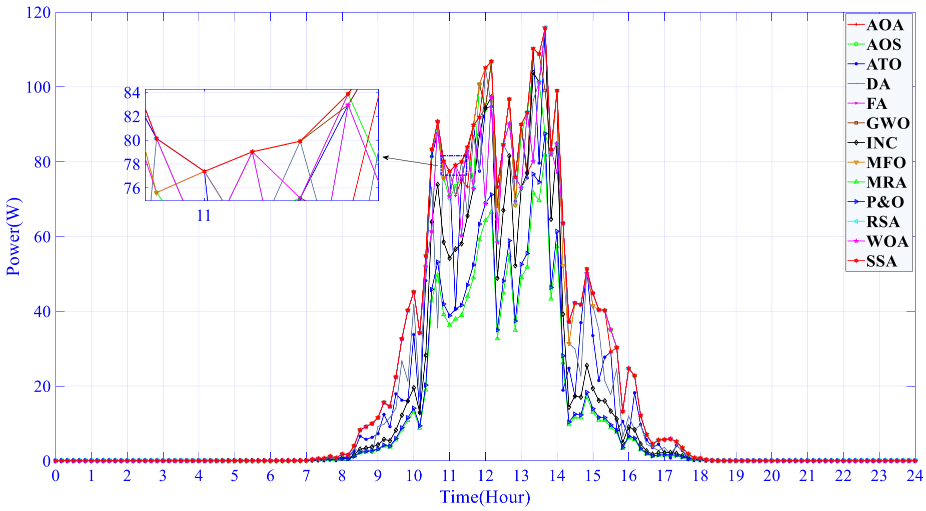

(a)

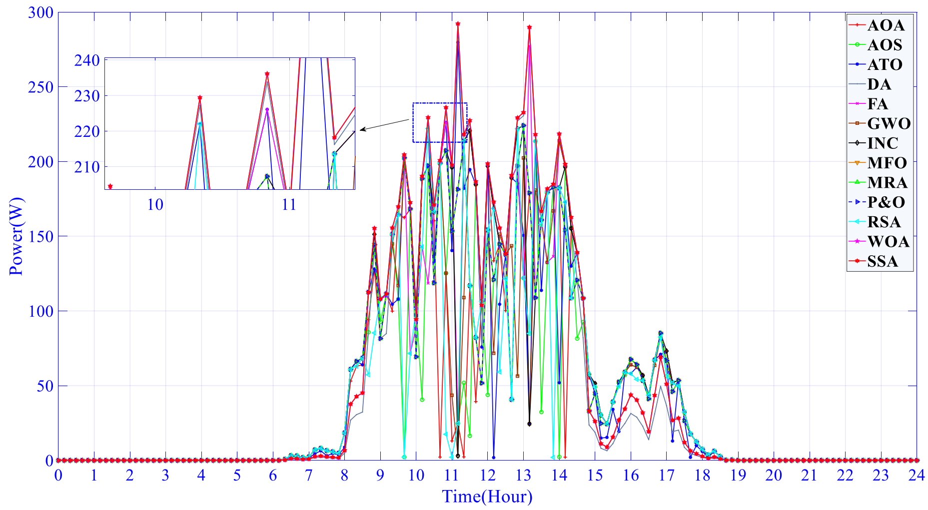

(b)

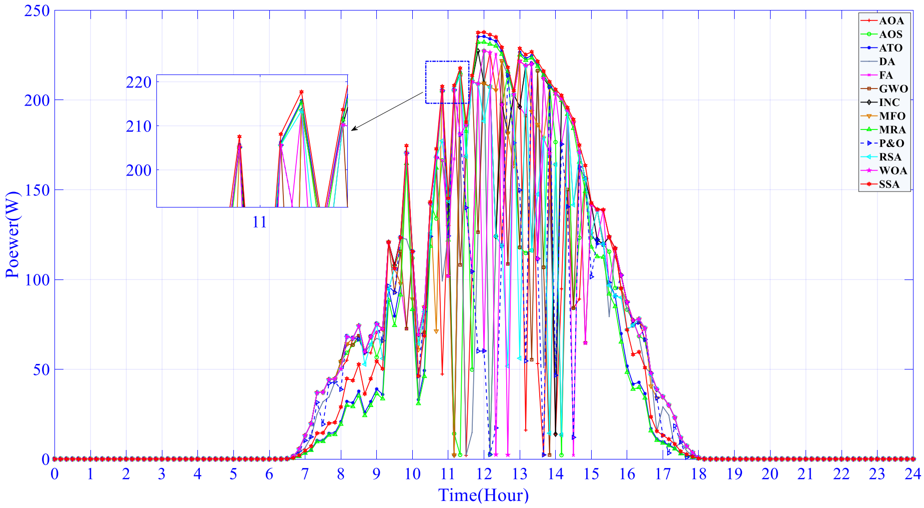

(c)

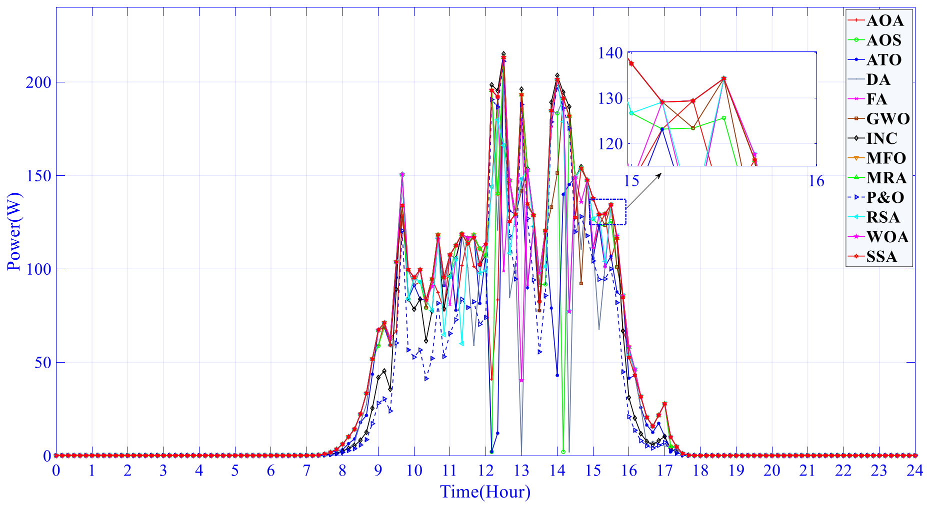

(d)

Fig. A5. Power obtained by PV subsystem on different typical days via thirteen methods. (a) Spring (b) Summer, (c) Autumn, and (d) Winter.

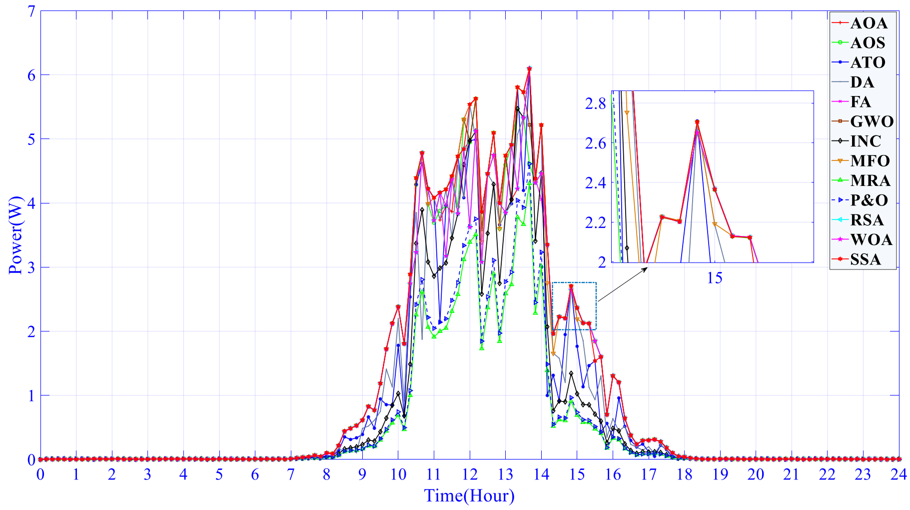

(a)

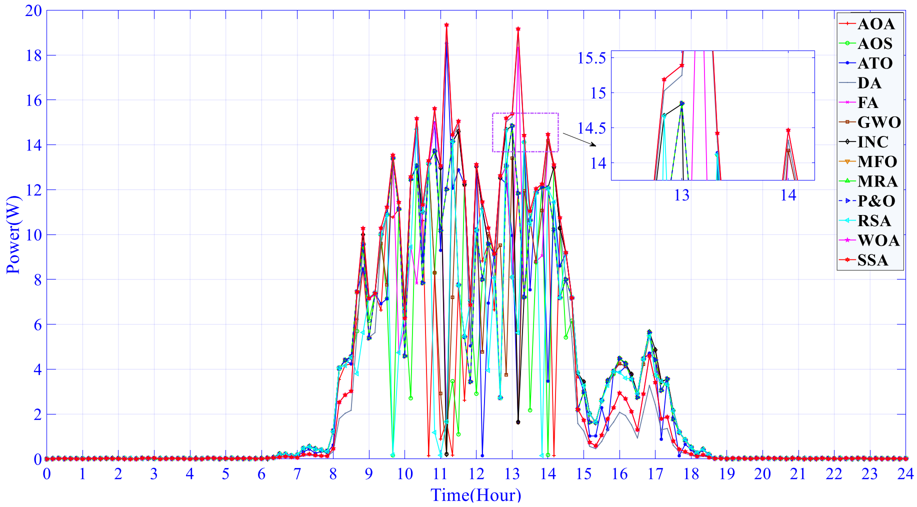

(b)

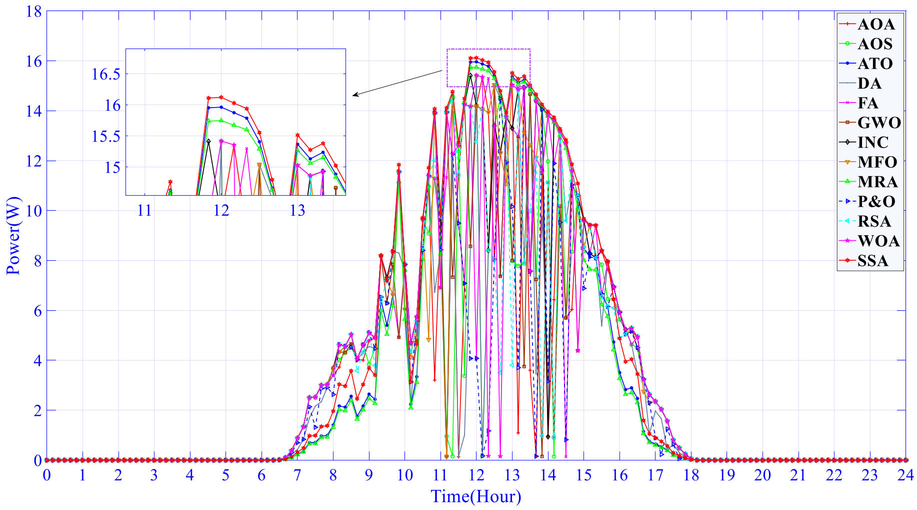

(c)

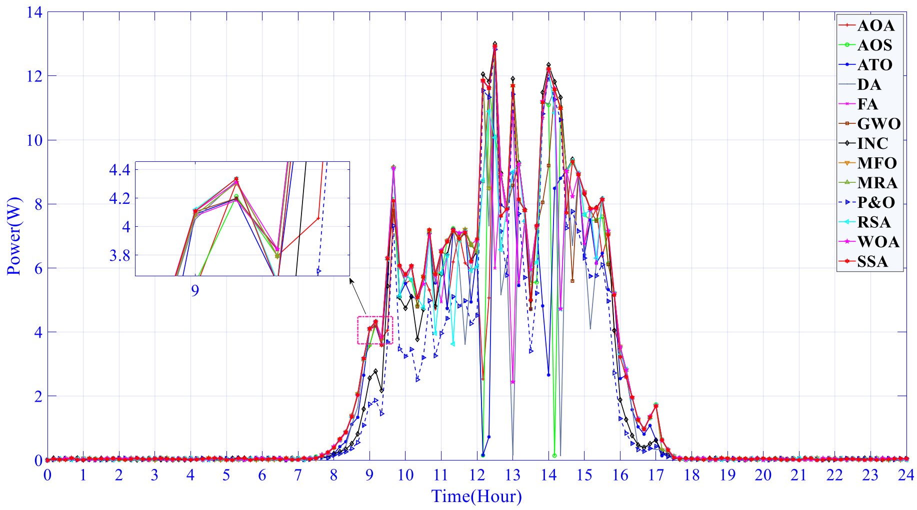

(d)

Fig. A6. Power obtained by TEG subsystem on different typical days via thirteen methods. (a) Spring (b) Summer, (c) Autumn, and (d) Winter.

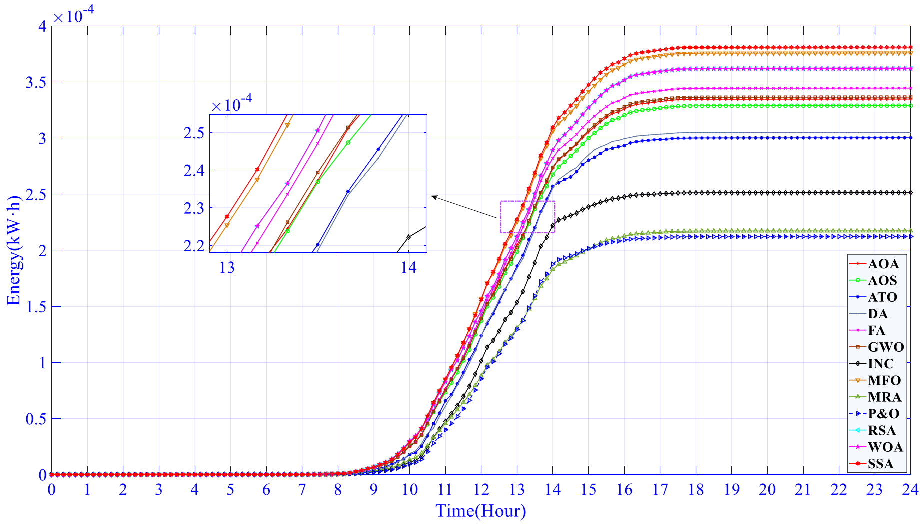

(a)

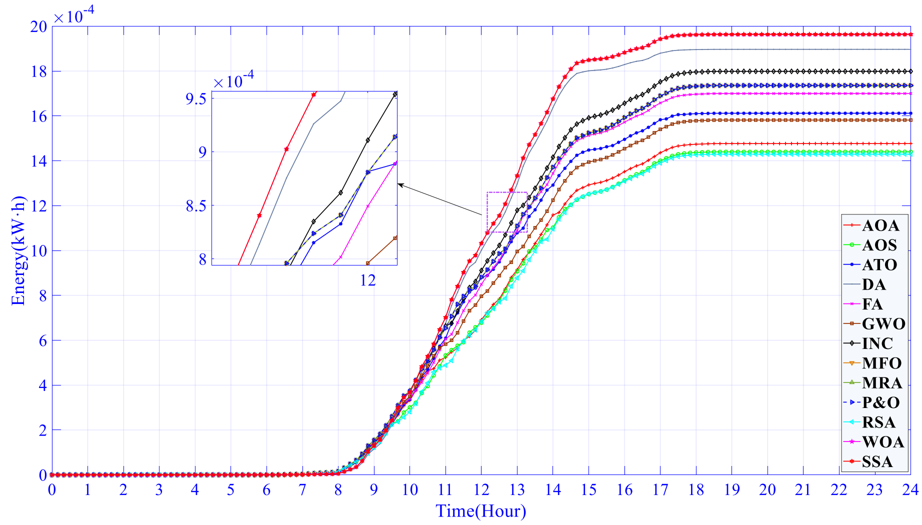

(b)

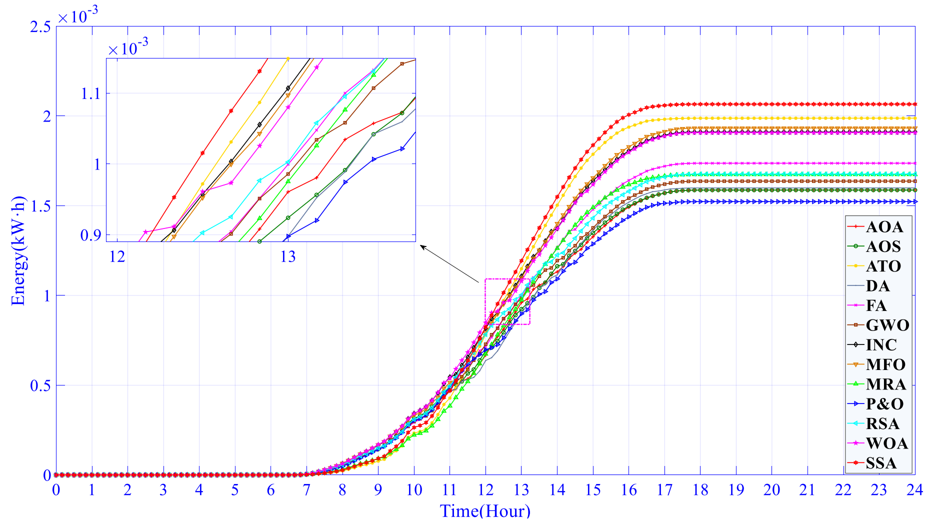

(c)

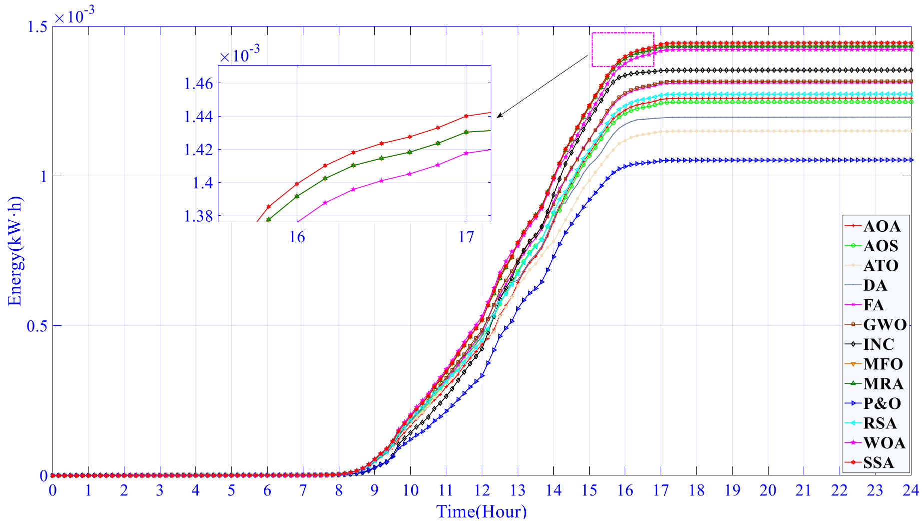

(d)

Fig. A7. Energy obtained by PV subsystem on different typical days via thirteen methods. (a) Spring (b) Summer, (c) Autumn, and (d) Winter.

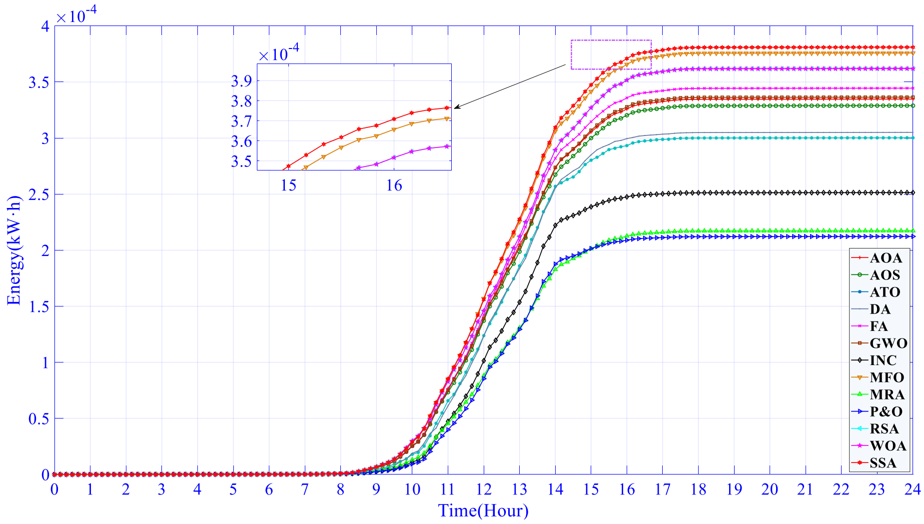

(a)

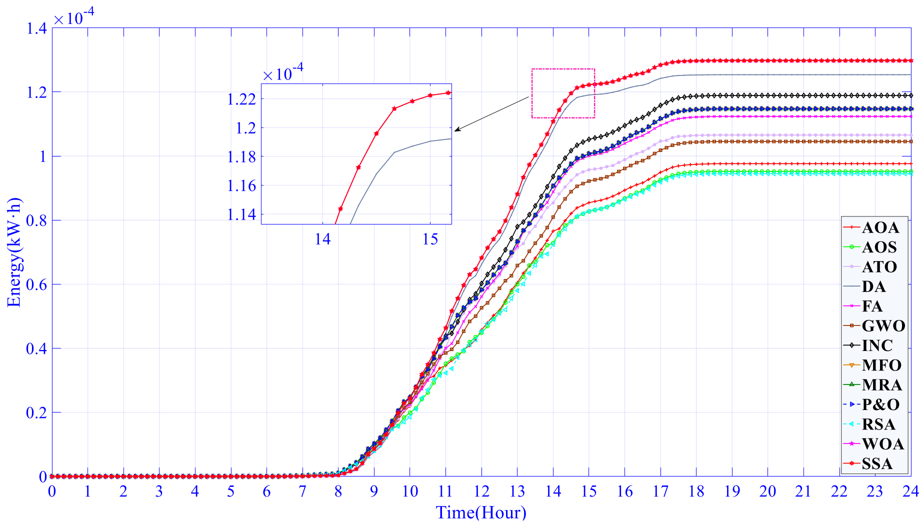

(b)

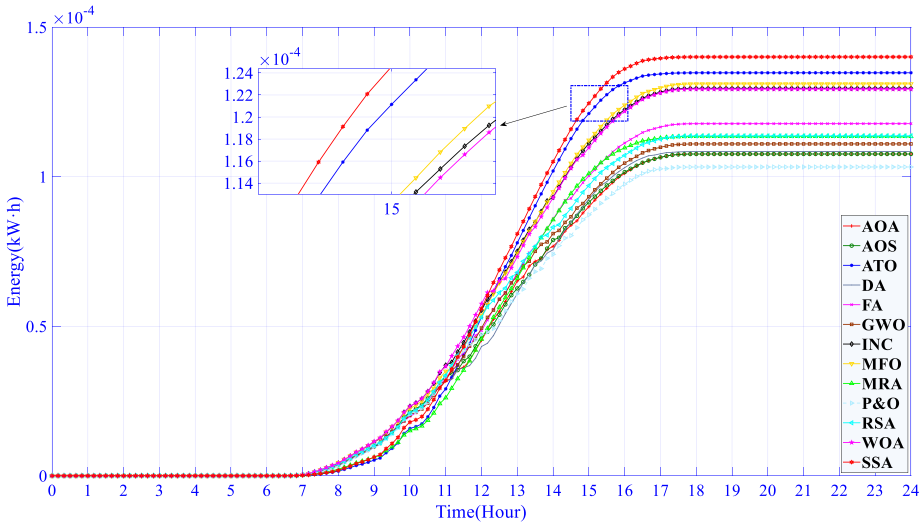

(c)

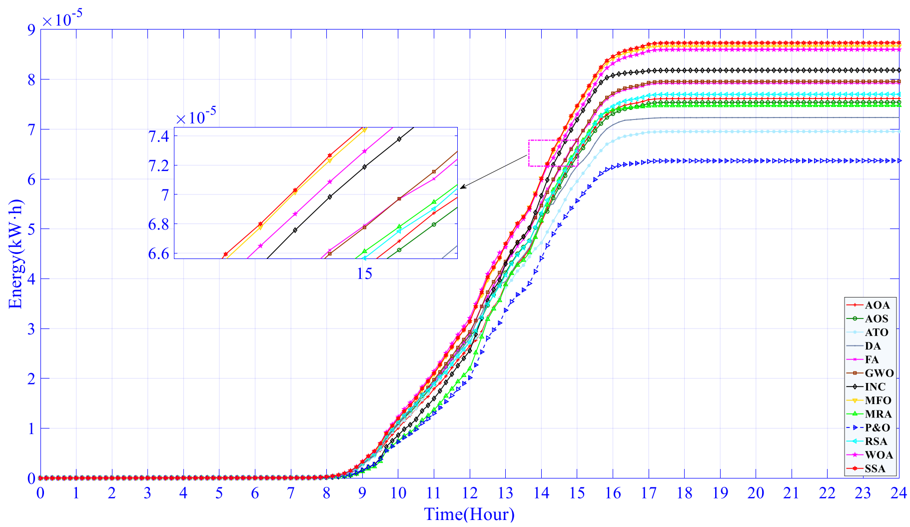

(d)

Fig. A8. Energy obtained by TEG subsystem on different typical days via thirteen methods. (a) Spring (b) Summer, (c) Autumn, and (d) Winter.

Reference

[1] Yang B, Zhang MT, Wang JB, et al. Interacted collective intelligence based energy harvesting of centralized thermoelectric generation systems under non-uniform temperature gradient. *Sustainable Energy Technologies and Assessments* **2021**, 48: 101600.

[2] Jamali E, Nobakhti MH, Ziapour BM, et al. Performance analysis of a novel model of photovoltaic PV-TEGs system enhanced with flat plate mirror reflectors. *Energy Conversion and Management* **2023**, 279: 116766.

[3] Chen YJ, Yang B, Guo ZX, et al. Dynamic reconfiguration for TEG systems under heterogeneous temperature distribution via adaptive coordinated seeker. *Protection and Control of Modern Power Systems* **2022**, 7(38): 1-19.

[4] Xu B, Zhang, G, Li, K. et al. Publisher Correction: Reactive power optimization of a distribution network with high-penetration of wind and solar renewable energy and electric vehicles. *Protection and Control of Modern Power Systems* **2023**, 8: 21.

[5] Yang B, Zhang MT, Zhang XS, et al. Fast atom search optimization based MPPT design of centralized thermoelectric generation system under heterogeneous temperature difference. *Journal of Cleaner Production*. **2020**, 248: 119301.
[6] Yang B, Yu T, Zhang X, et al. Dynamic leader based collective intelligence for maximum power point tracking of PV systems affected by partial shading condition. *Energy Conversion and Management* **2019**, 179:286-303.
[7] Allouhi A, Rehman S, Buker MS, et al. Up-to-date literature review on Solar PV systems: Technology progress, market status and R&D. *Journal of Cleaner Production* **2022**: 132339.
[8] Yang B, Zhu TJ, Wang JB, et al. Comprehensive overview of maximum power point tracking algorithms of PV systems under partial shading condition. *Journal of Cleaner Production* **2020**, 268: 121983.
[9] Yang B, Li YL, Li JL, Comprehensive summarization of solid oxide fuel cell: control: A state-of-the-art review. *Protection and Control of Modern Power Systems* **2022**: 7(36), 1-31.
[10] Dimri N, Tiwari A, Tiwari GN. Effect of thermoelectric cooler (TEC) integrated at the base of opaque photovoltaic (PV) module to enhance an overall electrical efficiency. *Solar Energy* **2018**, 166: 159-70.
[11] Ong KS, Naghavi MS, Lim C. Thermal and electrical performance of a hybrid design of a solar-thermoelectric system. *Energy Conversion and Management* **2017**, 133: 31-40.
[12] Yin E, Li Q, Xuan Y. Thermal resistance analysis and optimization of photovoltaic-thermoelectric hybrid system. *Energy Conversion and Management* **2017**, 143: 188-202.
[13] Lin J, Liao T, Lin B. Performance analysis and load matching of a photovoltaic-thermoelectric hybrid system. *Energy Conversion and Management* **2015**, 105: 891-899.
[14] Sundarraj, Pradeepkumar, et al. Experimental and theoretical analysis of a hybrid solar thermoelectric generator with forced convection cooling. *Journal of Physics D: Applied Physics* **2016**, 50(1): 015501.
[15] Babu C, Ponnambalam P. The theoretical performance evaluation of hybrid PV-TEG system. *Energy conversion and management* **2018**, 173: 450-460.
[16] Yin E, Li Q, Xuan Y. A novel optimal design method for concentration spectrum splitting photovoltaic–thermoelectric hybrid system. *Energy* **2018**, 163: 519-532.
[17] Shang L, Guo H, Zhu W. An improved MPPT control strategy based on incremental conductance algorithm. *Protection and Control of Modern Power Systems* **2020**, 5: 1-8.
[18] Altwallbah NMM, Radzi MAM, Azis N, et al. New perturb and observe algorithm based on trapezoidal rule: Uniform and partial shading conditions. *Energy Conversion and Management* **2022**, 264: 115738.
[19] Mirza AF, Ling Q, Javed MY, et al. Novel MPPT techniques for photovoltaic systems under uniform irradiance and Partial shading. *Solar Energy* **2019**, 184: 628-648.
[20] Verma V, Kane A, Singh B. Complementary performance enhancement of PV energy system through thermoelectric generation. *Renewable and Sustainable Energy Reviews* **2016**, 58: 1017-1026.
[21] Kwan TH, Wu X. The Lock-On Mechanism MPPT algorithm as applied to the hybrid photovoltaic cell and thermoelectric generator system. *Applied Energy* **2017**, 204: 873-886.
[22] Mirza AF, Mansoor M, Zerbakht K, et al. High-efficiency hybrid PV-TEG system with intelligent control to harvest maximum energy under various non-static operating conditions. *Journal of Cleaner Production* **2021**, 320: 128643.

[23] Khan MK, Zafar MH, Mansoor M, et al. Green energy extraction for sustainable development: A novel MPPT technique for hybrid PV-TEG system. *Sustainable Energy Technologies and Assessments* **2022**, 53: 102388.

[24] Fini MA, Gharapetian D, Asgari M. Efficiency improvement of hybrid PV-TEG system based on an energy, exergy, energy-economic and environmental analysis; experimental, mathematical and numerical approaches. *Energy Conversion and Management* **2022**, 265: 115767.

[25] Cotfas DT, Cotfas PA, Mahmoudinezhad S, et al. Critical factors and parameters for hybrid photovoltaic-thermoelectric systems; review. *Applied Thermal Engineering* **2022**, 215: 118977.

[26] Khan K, Rashid S, Mansoor M, et al. Data-driven green energy extraction: Machine learning-based MPPT control with efficient fault detection method for the hybrid PV-TEG system. *Energy Reports* **2023**, 9: 3604-3623.

[27] Skoplaki E, Palyvos JA. Operating temperature of photovoltaic modules: A survey of pertinent correlations. *Renewable energy* **2009**, 34(1): 23-29.

[28] Muzathik AM. Photovoltaic modules operating temperature estimation using a simple correlation. *International Journal of Energy Engineering* **2014**, 4(4): 151.

[29] Yang B, Ye HY, Wang JB, et al. PV arrays reconfiguration for partial shading mitigation: Recent advances, challenges and perspectives. *Energy Conversion and Management* **2021**, 247: 114738.

[30] Yang B, Shao R, Zhang M, et al. Socio-inspired democratic political algorithm for optimal PV array reconfiguration to mitigate partial shading. *Sustainable Energy Technologies and Assessments* **2021**, 48: 101627.

[31] Mirjalili S, Gandomi AH, Mirjalili SZ, et al. Salp Swarm Algorithm: A bio-inspired optimizer for engineering design problems. *Advances in engineering software* **2017**, 114: 163-191.

[32] Attou A, Massoum A, Saidi M. Photovoltaic power control using MPPT and boost converter. *Balkan journal of electrical & Computer Engineering* **2014**, 2(1): 23-27.

[33] Mirjalili S. Moth-flame optimization algorithm: A novel nature-inspired heuristic paradigm. *Knowledge-based systems* **2015**, 89: 228-249.

[34] Desuky AS, Cifci MA, Kausar S, et al. Mud Ring Algorithm: A new meta-heuristic optimization algorithm for solving mathematical and engineering challenges. *IEEE Access* **2022**, 10: 50448-50466.

[35] Mirjalili S, Mirjalili SM, Lewis A. Grey wolf optimizer. *Advances in engineering software* **2014**, 69: 46-61.

[36] Abualigah L, Abd Elaziz M, Sumari P, et al. Reptile Search Algorithm (RSA): A nature-inspired meta-heuristic optimizer. *Expert Systems with Applications* **2022**, 191: 116158.

[37] Devan P, Hussin FA, Ibrahim RB, et al. An arithmetic-trigonometric optimization algorithm with application for control of real-time pressure process plant. *Sensors* **2022**, 22(2): 617.

[38] Yang XS, He X. Firefly algorithm: recent advances and applications. *International journal of swarm intelligence* **2013**, 1(1): 36-50.

[39] Mirjalili S, Lewis A. The whale optimization algorithm. *Advances in engineering software* **2016**, 95: 51-67.

[40] Yang B, Zhong LN, Yu Tao, et al. Novel bio-inspired memetic salp swarm algorithm and application to MPPT for PV systems considering partial shading condition. *Journal of Cleaner Production* **2019**, 215: 1203-1222.

[41] Ravita L, Kaushik SC. Modeling and performance analysis of a concentrated photovoltaic–thermoelectric hybrid power generation system. *Energy Conversion and Management* **2016**, 115:

288-298.

[42] Xuan XC, Ng KC, Yap C, et al. The maximum temperature difference and polar characteristic of two-stage thermoelectric coolers. *Cryogenics* **2002**, 42: 273-278.